

Direct electrical modulation of surface response in a single plasmonic nanoresonator

Luka Zurak,^{1,*} Christian Wolff,² Jessica Meier,¹ René Kulloock,¹ N. Asger Mortensen,^{2,3} Bert Hecht,¹ and Thorsten Feichtner^{1,†}

¹*Nano-Optics and Biophotonics Group, Experimental Physics 5,
Institute of Physics, University of Würzburg, Germany*

²*POLIMA – Center for Polariton-driven Light-Matter Interactions,
University of Southern Denmark, Campusvej 55, DK-5230 Odense M, Denmark*

³*Danish Institute for Advanced Study, University of Southern Denmark, Campusvej 55, DK-5230 Odense M, Denmark*

Classical electrodynamics is suitable to describe the optical response of macroscopic systems, where bulk properties play a dominant role and the boundary between two materials is treated as infinitesimally thin. However, due to the quantum nature of electrons, interface acquires a finite thickness. To account for the optical response of non-classical surface effects within the framework of Maxwell's equations, classical boundary conditions are supplemented with surface-response functions, better known as Feibelman d -parameters. Surface response has a prominent impact on electrodynamics of systems with strong field localization at the interface region, which is typically encountered in noble metal nanoparticles supporting surface plasmon polaritons. However, studying surface response is challenging as it necessitates the sub-nanometer control of critical geometrical features, such as the gap size in a dimer antenna, while minimizing effects of surface roughness and uncertainties in morphology, which also contribute to the broadening and spectral shifting of plasmonic resonances. In contrast, electrical gating is a convenient control knob since the static screening charges are confined exclusively to the surface, which alleviates the need for precise control over the morphology. Here, we study the perturbation of Feibelman d -parameters by direct electric charging of a single plasmonic nanoresonator and investigate the resulting changes of the resonance in experiment and theory. The measured change of the resonance frequency matches the one predicted theoretically by assuming a perturbation of the tangential surface current. However, we also observe an unforeseen change in the resonance width. Adding electrons to the surface of a plasmonic nanoresonator leads to a narrowing of the resonance, i.e. to reduced losses which cannot be explained by electron spill-out within the local-response approximation (LRA). Such an effect is likely caused by nonlocality and the anisotropy of the perturbed local permittivity. Our findings open up possibilities to reduce losses in plasmonic resonators and to develop ultrafast and extremely small electrically driven plasmonic modulators and metasurfaces by leveraging electrical control over non-classical surface effects.

I. INTRODUCTION

The interaction between free electrons at a metal surface and electromagnetic fields at optical frequencies gives rise to surface plasmon polaritons (SPPs), which are strongly coupled states of light and charge-density oscillations [1]. When SPP waves are confined to a finite sized objects, they exhibit resonances with large field enhancements in the vicinity of maxima in the surface-charge density [2]. In addition, as the SPP resonances depend on the object's shape, they can be easily shifted across the spectrum [3]. These practical properties of localized plasmonic resonances have been extensively studied and widely utilized [4–9]. However, with the advancement of nanofabrication and computational methods, fundamental limitations of plasmonic systems, imposed by the non-classical properties of free electrons at the surface, have moved into the focus of interest [10–21]. Reduced field enhancement, accompanied by broadening and spectral shifting of resonances, are caused by electronic spill-out effect [19, 22], nonlocality [23], and Landau damping [24–26]. The analysis of such non-classical effects is based on correlating spectral and morphology measurements. This involves using the morphology as input for simulations based on the LRA, assuming bulk material properties, and subsequently attributing observed spectral deviations to the nonlocal response [17, 18, 20, 21]. However, obtaining accurate nanoscale information on morphology and possible surface roughness remains a challenge. Likewise, for nanofabrication it is difficult to systematically vary a single parameter, such as the gap size in a dimer, while minimizing sample-to-sample fluctuations in other geometry parameters. Apart from manipulating the geometry, the plasmon resonance can be influenced by varying the density of the electron gas. This feature is particularly exploited in dilute systems, such as graphene plasmonics [27–29], but often disregarded in metallic nanoresonators with higher carrier densities. In such systems, which exhibit small capacitances, even for sizable bias voltages, only a relatively small number of electrons can be added to a resonator. Various methods have been employed to experimentally investigate and enhance electrical tuning of plasmonic nanoresonators, such as embedding resonators in a chemical reductant or an ion gel, which has resulted in a significant increase in the capacitance of the system [30–38]. However, these approaches have limitations, including slow operation and inconclusive results. Hysteresis has been observed in some cases, likely due to double-layer formation or electrochemistry at the metal surface, suggesting different origins of the observed effects beyond charg-

* luka.zurak@physik.uni-wuerzburg.de

† thorsten.feichtner@physik.uni-wuerzburg.de

ing [32–34, 36]. Moreover, only few studies have modeled the influence of charging on the optical response as a surface effect [39–41], while a typical approach is to assume a change in the bulk properties (see Supplementary Section 1.2) [31, 32, 42]. However, none of these studies have analyzed the observed results in terms of surface-response functions, which could provide a deeper insight and subsequently open routes to enhance the electrical tuning. Achieving a large modulation would unlock the full potential of active plasmonic systems and enable the development of ultrafast and ultrasmall electrically driven optical modulators and tunable metamaterials [43]. Additionally, control over the electron spill-out effect has the potential to amplify nonlinear phenomena associated with the surface of plasmonic materials [44–47]. Moreover, the appearance of a plasmoelectric potential in plasmonic nanostructures is fundamentally reliant on electrical tunability of plasmonic resonances [42].

In this study, we investigate the effect of adding charges to the surface of a single electrically connected SPP resonator in both theory and experiment. We use Feibelman d -parameters to study the influence of added electrons by conducting density-functional theory (DFT) calculations within the jellium approximation [48] to obtain voltage-induced perturbations of the d -parameters under the LRA. We measure the relative change in scattering for an applied potential of ± 10 V, and subsequently determine the induced changes in the eigenfrequency of the nanoresonator. The observed change in the resonance frequency follows the theoretically anticipated trend. However, we also observe a change in the resonance width, which is not predicted with the LRA. We attribute this observation to effects not considered in our model, such as e.g. the perturbation of conductivity via surface-states, anisotropy of the local permittivity, or nonlocal effects hidden in the perpendicular component of the d -parameters.

II. SURFACE-RESPONSE FUNCTIONS

Bohren and Hunt [39] made one of the initial attempts to model how adding electrons to the surface of a plasmonic nanoresonator affected the resonance. They assumed that, in the picture of classical electrodynamics, added electrons modify the surface conductivity σ_s and consequently perturb the in-plane surface current $\mathbf{K} = \sigma_s \mathbf{E}_{\parallel}$ driven by the tangential component of electric field \mathbf{E}_{\parallel} . However, to fully capture optical properties of electrons at the surface one has to take into account various non-classical effects. First of all, electron spill-out causes the surface to acquire a finite thickness and leads to an out-of-plane response. Other quantum effects which influence the electronic response at the surface are nonlocality, Landau damping and conduction through surface-states [49, 50]. All such effects can be accounted for by Feibelman d -parameters [10, 49]. The d -parameters, d_{\perp} and d_{\parallel} , are centroids of the induced charge density and of the normal derivative of the tangential current, respectively [10] (see Supplementary Section 1.4). Hence, as demonstrated by Christensen *et al.* [51], d -parameters describe the surface po-

larization

$$\mathbf{P}_s = \boldsymbol{\pi} + i\omega^{-1}\mathbf{K}. \quad (1)$$

Out-of-plane electron oscillation, proportional to d_{\perp} , is described via the dipole density $\boldsymbol{\pi} = \epsilon_0 d_{\perp} \Delta E_{\perp} \hat{x}_{\perp}$, where ϵ_0 is the free-space permittivity, E_{\perp} is the perpendicular component of electric field, and \hat{x}_{\perp} is normal unit vector. The parallel component d_{\parallel} contributes to an in-plane surface current $\mathbf{K} = i\omega d_{\parallel} \Delta \mathbf{D}_{\parallel}$ as already discussed by Bohren and Hunt, where \mathbf{D}_{\parallel} is the tangential component of displacement field.

If we assume a simple harmonic oscillator as a model for a plasmonic nanoresonator (see Fig. 1 a), the associated Lorentzian $L(\omega; \omega_r, \gamma_r)$ can be described by a complex eigenfrequency $\tilde{\omega}_r = \omega_r - i\gamma_r/2$ [52]. The real part corresponds to the resonance frequency, while the imaginary part $\gamma_r/2$ describes the attenuation of the system. It contains radiation as well as Ohmic losses.

Surface effects described by the Feibelman d -parameters lead to a change of the plasmonic nanoresonator's eigenfrequency $\Delta\tilde{\omega}_r$, which is directly related to the surface polarization via the integral [53]

$$\Delta\tilde{\omega}_r = -\tilde{\omega}_{r0} \int_s \mathbf{E}^{(0)} \cdot \mathbf{P}_s^{(0)} ds, \quad (2)$$

where s denotes the surface of the resonator. Here, $\mathbf{P}_s^{(0)}$ and $\mathbf{E}^{(0)}$ are evaluated at the unperturbed eigenfrequency $\tilde{\omega}_{r0}$ obtained by assuming classical piecewise constant material properties, neglecting any non-classical effects introduced via the surface polarization $\mathbf{P}_s^{(0)}$. Therefore, the experimentally observed eigenfrequency of an uncharged plasmonic nanoresonator is given as a $\tilde{\omega}_r = \tilde{\omega}_{r0} + \Delta\tilde{\omega}_r$. Furthermore, in the case of a controlled perturbation, a small shift in the spectral position of the resonance frequency $\Delta\omega_r$ produces a distinct pattern in the relative change of the resonance, as depicted in Fig. 1b. It can be easily differentiated from the relative change caused by the perturbation of the width of the resonance $\Delta\gamma_r$ (see Supplementary Section 1.1).

We use the same formalism to describe the charge-induced eigenfrequency shifts of a single gold nanoresonator residing on top of a glass substrate as shown in Fig. 1c. At any point on the surface of the nanoresonator \mathbf{r}_s , an applied voltage V will introduce a change in equilibrium electron density and locally perturb surface-response functions

$$d_{\perp}(\mathbf{r}_s, V) \simeq d_{\perp} + \frac{\partial d_{\perp}(\mathbf{r}_s, V)}{\partial V} V, \quad (3a)$$

$$d_{\parallel}(\mathbf{r}_s, V) \simeq d_{\parallel} + \frac{\partial d_{\parallel}(\mathbf{r}_s, V)}{\partial V} V. \quad (3b)$$

The perturbed d -parameters will lead to a local change of the surface polarization $\Delta\mathbf{P}_s(\mathbf{r}_s, V)$ (see Fig. 1e), which will introduce a voltage-induced change in the system's eigenfrequency $\Delta\tilde{\omega}_r(V)$ in accordance with Eq. (2). Experimentally, changes in the system's eigenfrequency $\Delta\tilde{\omega}_r(V)$ can be obtained by inspecting the relative change of scattering $\Delta S(V)/S_0$ (as shown in Fig. 1b), where $\Delta S(V)$ is the voltage-induced change in scattering signal and S_0 is the scattering signal of the uncharged system – the scattering signal is defined as normalized scattering cross section $S \propto \sigma_{\text{sca}}$.

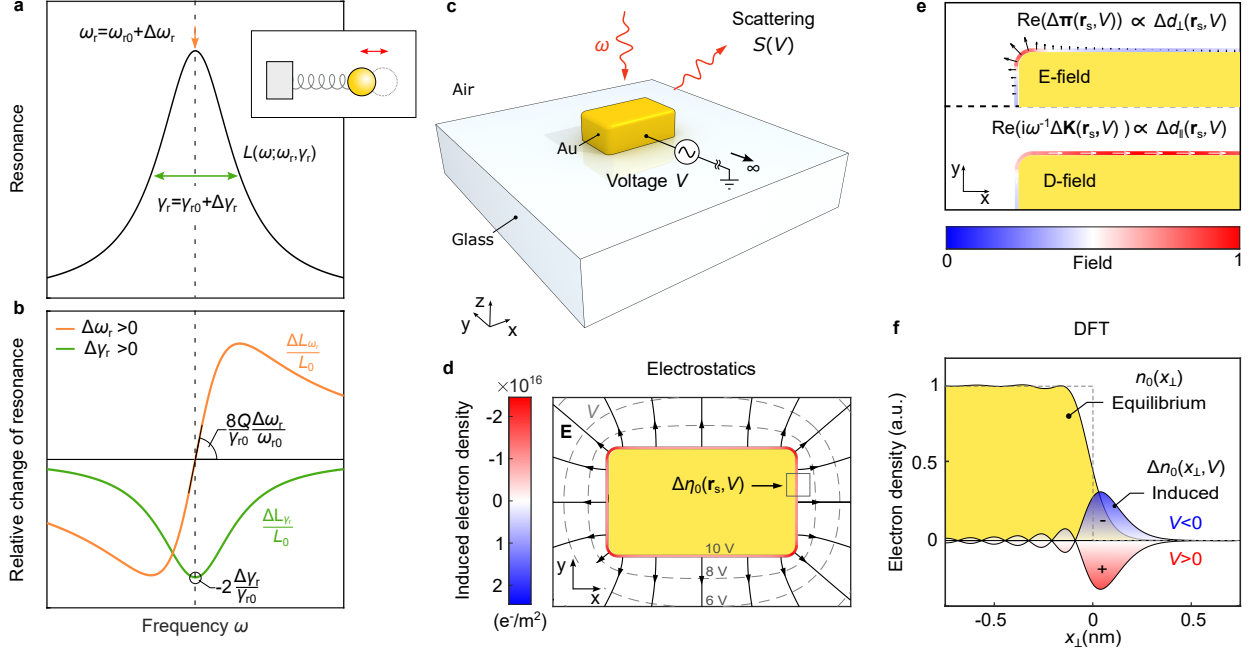


FIG. 1. **Influence of electrostatically induced surface charge on optical response of plasmonic nanoresonators.** **a**, Model of a harmonic oscillator and a corresponding resonance with Lorentzian line shape $L(\omega; \omega_r, \gamma_r)$ described with resonant frequency ω_r and width γ_r . **b**, Small perturbations of $\Delta\omega_r > 0$, or $\Delta\gamma_r > 0$, lead to distinct relative changes of the resonance represented by the orange curve ($\Delta\omega_r$) and the green curve ($\Delta\gamma_r$), respectively. **c**, Sketch of the system under research; a rectangular gold (Au) nanoresonator is placed on top of a glass substrate. The applied electric potential V induces a change in the resonance which is detected by recording the scattering signal $S(V)$ as a function of the photon energy $\hbar\omega$ and the applied potential. **d**, Simulated static electric field lines at half of the antenna height (black arrowed lines) and contours of electric potential (gray dashed lines) for a 10 V equipotential at the surface of the structure. Excess electrons are non-uniformly distributed across the surface, represented by the induced surface electron density $\Delta\eta_0(\mathbf{r}_s, V)$ (surface color). **e**, The change in electron density at the surface perturbs the d -parameters given with Eq. (5a) and (5b), and in turn the optical response of the system by altering the surface polarization $\mathbf{P}_s(\mathbf{r}_s, V)$ (see Eq. (2)). **f**, Equilibrium and induced electron density distributions at the gold-air interface calculated using a Wigner–Seitz radius of $r_s/a_0 = 3.18$ for the jellium description.

To theoretically inspect the strength of perturbations at some point on the surface \mathbf{r}_s , in a first approximation, we calculate the perturbation coefficients $\partial_V d_\perp$ and $\partial_V d_\parallel$ resulting from electron spill-out under the LRA assuming a position-dependent plasma frequency $\omega_p(x_\perp, V) = \omega_{p0} \sqrt{n_0(x_\perp, V)/n_0}$, where ω_{p0} is the unperturbed plasma frequency and n_0 is the bulk density of free electrons. Therefore, the optical properties at position x_\perp , perpendicular to the interface, are described with the position-dependent local permittivity

$$\varepsilon_{\text{LRA}}(x_\perp, V) = \varepsilon_b(x_\perp) - \frac{\omega_{p0}^2}{\omega^2 + i\gamma\omega} \frac{n_0(x_\perp, V)}{n_0}, \quad (4)$$

where the equilibrium electron density perpendicular to the surface of the metal is given as $n_0(x_\perp, V) = n_0(x_\perp) + \Delta n_0(x_\perp, V)$. Here, $n_0(x_\perp)$ is the equilibrium electron density of an uncharged system and $\Delta n_0(x_\perp, V)$ is the voltage-induced electron density. $\varepsilon_b(x_\perp)$ is the position dependent background permittivity – in the bulk gold it is dominated by the interband contributions and subsequently transitions to the permittivity of the dielectric outside gold. For simplicity, we omit that the electron response at the surface is anisotropic – it is expected that the equation-of-motion perpendicular to the in-

terface contains additional terms that describe the influence of the boundary. Therefore, assuming isotropy of the local permittivity, according to Ref. 22, the d -parameter perturbation coefficients can be expressed in integral form as

$$\frac{\partial d_\perp}{\partial V} = \frac{\varepsilon_d \varepsilon_m}{\varepsilon_m - \varepsilon_d} \int_{-\infty}^{\infty} dx_\perp \frac{1}{\varepsilon_{\text{LRA}}^2(x_\perp, V)} \frac{\partial}{\partial V} \varepsilon_{\text{LRA}}(x_\perp, V), \quad (5a)$$

$$\frac{\partial d_\parallel}{\partial V} = \frac{1}{\varepsilon_m - \varepsilon_d} \int_{-\infty}^{\infty} dx_\perp \frac{\partial}{\partial V} \varepsilon_{\text{LRA}}(x_\perp, V). \quad (5b)$$

Here, ε_m and ε_d are permittivities of the metal and surrounding dielectric, respectively (for a detailed derivation see Supplementary Section 1.4).

For both components, the integrands in Eqs. (5a) and (5b) depend on the induced electron density $\Delta n_0(x_\perp, V)$, which can be related to the classical induced surface electron density $\Delta\eta_0(V)$ via the integral

$$\int dx_\perp \Delta n_0(x_\perp, V) = \Delta\eta_0(V). \quad (6)$$

The voltage-induced surface electron density can be obtained

from the discontinuity of the normal component of the static displacement field $D_{\perp} = \kappa E_{\perp}$, where E_{\perp} is the normal component of the static electric field (see Fig. 1d) in the dielectric and κ is the static dielectric constant. Furthermore, we can express the induced surface electron density in terms of a surface capacitance C_s as $\Delta n_0(V) \approx C_s V / q_e$, where q_e is the electron charge, showing explicitly the dependency on the applied potential. Furthermore, this implies that we can represent the induced electron density as

$$\Delta n_0(x_{\perp}, V) \approx p(x_{\perp}) \frac{C_s V}{q_e}, \quad (7)$$

where $p(x_{\perp})$ is the probability distribution of the induced electron density per unit length, which carries the shape of the induced electron density and satisfies the normalization condition $\int dx_{\perp} p(x_{\perp}) = 1$.

In the case of the d_{\parallel} component, using Eq. (4) for the evaluation of Eq. (5b) reduces to the evaluation of the partial derivative with respect to voltage of the integral given with Eq. (6). This expression can be evaluated by employing Eq. (7), which implies that the perturbation is independent of the shape of the induced electron density and only depends on the amount of the induced charge. Therefore, the perturbation coefficient can be expressed analytically with a purely classical term

$$\frac{\partial d_{\parallel}(\mathbf{r}_s, V)}{\partial V} \approx \frac{1}{\epsilon_d - \epsilon_m} \frac{\omega_p^2}{\omega^2 + i\gamma\omega} \frac{C_s(\mathbf{r}_s)}{q_e} \frac{1}{n_0}, \quad (8)$$

where the surface position dependency has been reintroduced through the surface capacitance $C_s(\mathbf{r}_s)$. One can show that the perturbed d_{\parallel} parameter directly leads to a perturbed surface conductivity $\Delta\sigma_s \propto \Delta d_{\parallel}$, the same result as provided by the classical model of Bohren and Hunt (for a detailed discussion see Supplementary Section 1.7).

In addition to the perturbation of the surface conductivity resulting from the bulk electrons, other non-classical effects, such as conduction through surface-states, can also impact the d_{\parallel} perturbation coefficient [49, 50]. On the other hand, nonlocal effects are primarily associated with regions of high electric field gradients where electrons tend to accumulate [23]. Since the parallel component of the electric field gives rise to tangential surface currents, nonlocal contributions to this component are typically considered negligible.

In the case of the d_{\perp} component, by inserting Eq. (7) for the induced electron density into Eq. (4), the surface position dependency carried by the surface capacitance can be taken outside the integral in Eq. (5a) which results in the following expression

$$\frac{\partial d_{\perp}(\mathbf{r}_s, V)}{\partial V} \approx \frac{\epsilon_d \epsilon_m}{\epsilon_d - \epsilon_m} \frac{\omega_p^2}{\omega^2 + i\gamma\omega} \frac{C_s(\mathbf{r}_s)}{q_e} \frac{1}{n_0} \int_{-\infty}^{\infty} dx_{\perp} \frac{p(x_{\perp})}{\epsilon_{\text{LRA}}^2(x_{\perp})}. \quad (9)$$

Evaluation of the integral in Eq. (9) is not trivial since it depends on the shape of the induced electron density and the local permittivity. For simplicity, we assume that the background permittivity follows the distribution of the equilibrium

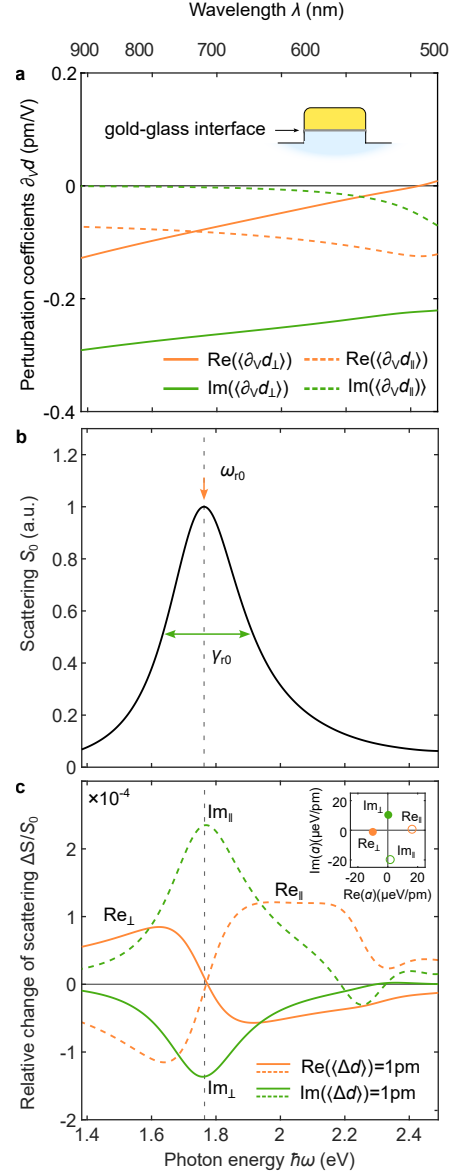


FIG. 2. Influence of d -parameter perturbations on a plasmonic resonance. **a**, Spectral dependency of surface averaged d -parameter perturbation coefficients for the gold-glass interface. The d_{\perp} component contributions are depicted with a solid lines, while the d_{\parallel} component are represented with dashed lines. Real parts are given in orange, and imaginary parts in green. **b**, Calculated unperturbed scattering spectrum S_0 , normalized to the maximum value, for the corresponding resonator with denoted unperturbed resonance position ω_{r0} and unperturbed resonance width γ_{r0} . **c**, Calculated relative change of scattering $\Delta S/S_0$ for 1 pm of introduced surface-averaged d -parameter perturbations. The inset shows the strength a of the eigenfrequency perturbations.

electron density (see Fig. 1f), which is derived from DFT calculations using the jellium approximation. Subsequently, as one transitions from the metal to the dielectric, the equilibrium electron density smoothly changes between the bulk value and zero. This results in a position where the local permittivity

(real part) crosses zero. Therefore, accurately evaluating the integral in Eq. (5a) necessitates a precise knowledge of the shape of the permittivity in the vicinity of this position (for more details refer to Supplementary Section 1.5).

III. SIMULATIONS

To assess the size of the perturbation coefficients given with Eqs. (8) and (9), we perform DFT calculations for a thin slab of jellium (8 nm), and electrostatic simulations for a 140 nm long, 80 nm wide and 50 nm high gold nanoresonator, and evaluate the spectrally dependent, interface averaged d -parameter perturbation coefficients as shown in Fig. 2a. Real and imaginary parts for all the perturbation coefficients exhibit negative values and show gradual variations across the spectrum. These coefficients have magnitudes on the order of 0.1 pm/V. Therefore, for typical voltages of around 10 V, the resulting perturbations $\langle \Delta d \rangle = \langle \partial_V d \rangle V$ will be approximately 1 pm. Negative signs in the real parts are expected, since for a positive bias we deplete the surface from polarizable material, effectively reducing the size of the resonator. Although in Fig. 2a we show only the case of the gold-glass interface, the result is similar for the gold-air interface.

Next, we examine the extent to which each component of the d -parameters perturbs the eigenfrequency $\tilde{\omega}_r$ of the nanoresonator, as described by Eq. (2). First, numerical simulations are conducted to solve Maxwell's equations at optical frequencies from where we obtain the scattering resonance as shown in Fig. 2b. In order to ensure treatments of simulations and experiments on an equal footing, the unperturbed resonance position ω_{r0} and width γ_{r0} are obtained by fitting a Lorentzian line shape with a linear background to the simulated scattering spectrum S_0 . In the second step, we vary each of the d -parameters independently by 1 pm of surface-averaged value and calculate the relative change of scattering $\Delta S/S_0$ using mesoscopic boundary conditions (see Fig. 2c) [20, 51, 54]. Subsequently, the perturbation strengths $a = \hbar \Delta \tilde{\omega}_r / \langle d \rangle$ are retrieved by fitting the relative change of the Lorentzian line shape $\Delta L/L_0$ to the calculated relative change of scattering with changes in resonance position $\Delta \omega_r$ and resonance width $\Delta \gamma_r$ as fitting parameters (refer to Supplementary Figure S3 for more details). We can see that for a real part perturbation of 1 pm in the d_{\parallel}/d_{\perp} component (denoted as $\text{Re}_{\parallel}/\text{Re}_{\perp}$ in Fig. 2c, respectively) we obtain dispersive curves with maximal changes on the slopes of the resonance, and a zero-crossing point almost perfectly aligned with the position of the resonance frequency. These characteristic shapes of the relative changes are produced by a change in the resonance position (compare orange curves in Fig. 2c and Fig. 1b), which is reflected in an almost purely real perturbation strengths of $a = (16.26 + 0.70i) \mu\text{eV}/\text{pm}$ and $a = (-10.0 - 0.87i) \mu\text{eV}/\text{pm}$ for the d_{\parallel} and d_{\perp} component, respectively. The perturbation strengths are shown in the inset of Fig. 2c. Moreover, introducing a perturbation of 1 pm to the imaginary part of the d_{\parallel}/d_{\perp} component (denoted as $\text{Im}_{\parallel}/\text{Im}_{\perp}$ in Fig. 2c) predominantly influences the width of the resonance (compare green curves in Fig. 2c and Fig. 1b), and yields purely imagi-

nary perturbation strengths of $a = (1.6 - 16.85i) \mu\text{eV}/\text{pm}$ and $a = (0.34 + 9.75i) \mu\text{eV}/\text{pm}$ for the d_{\parallel} and d_{\perp} component, respectively. Due to the presence of the perpendicular component of the optical electric field solely at the edges of the gold-glass interface, a perturbation in the d_{\perp} component has a relatively smaller impact on the resonance compared to an equivalent perturbation in the d_{\parallel} component as expected from Eq. (2).

IV. EXPERIMENT

To experimentally investigate the effect of charging on the plasmonic resonance, we conducted dark-field scattering measurements on an electrically connected nanoresonator, as depicted in Fig. 3a. The plasmonic resonators under investigation are fabricated from 50 nm thick single crystalline gold microplatelets [55], using a two-step focused ion beam (FIB) milling process. The first step involved Ga-FIB to create the rough shape of the resonator and connector. Then, He-FIB was employed to refine the structure's final shape with precision, as shown in the inset of Fig. 3b (similar to the procedure in Ref. 56). The shape of the resonance was probed with a supercontinuum white-light laser spectrally tuned using a narrowband filter, with its collimated beam polarized along the long-axis of the resonator. The scattering signal S is proportional to the ratio of the power scattered by the structure P and the incoming intensity I (see Supplementary Section 2.3). In Fig. 3b, we plot the normalized scattering spectrum of a 140 nm long and 80 nm wide resonator. As the expected change in scattering for a few volts of applied potential is only a few parts in ten thousand (estimated from Fig. 2a and 2c), we drive the system using a sinusoidal voltage with an amplitude V at frequency ν_0 . We employed a phase-sensitive lock-in amplifier to detect both the amplitude ΔP and the phase ϕ of the voltage-modulated scattered power, as illustrated in Fig. 3a. The unperturbed scattered power P_0 was recorded using a powermeter placed in one of the branches of the detection system (see Supplementary Figure S4). The ground electrode is positioned 2 μm away from the structure, resulting in self-capacitive charging that is comparable to theoretical predictions. By repeating the measurement across the spectrum, we obtain the spectral shape of the relative change of scattering (see Fig. 3c). In this exemplary case, at a linear frequency of 24 kHz, for +10 V of applied voltage, we observe a redshift of the peak position of $\hbar \Delta \omega_r = (-25 \pm 4) \mu\text{eV}$ and a resonance broadening of $\hbar \Delta \gamma_r = (19 \pm 3) \mu\text{eV}$. Therefore, equivalently for -10 V we observe blueshift and resonance narrowing of the same magnitude. Furthermore, the lock-in signal appears only at the first harmonic and has a purely in-phase component ($\phi = \{0, \pi\}$), in line with a charge-induced effect that is expected to have a linear dependence for low voltages (for more details see Supplementary Figure S8).

In Fig. 3e we show the simulated curves for the relative change of scattering obtained by summing contributions from each component of the d -parameters for +10 V of applied potential (see Supplementary Section 1.8). We can see that the perturbation in the d_{\parallel} component, which is regarded as

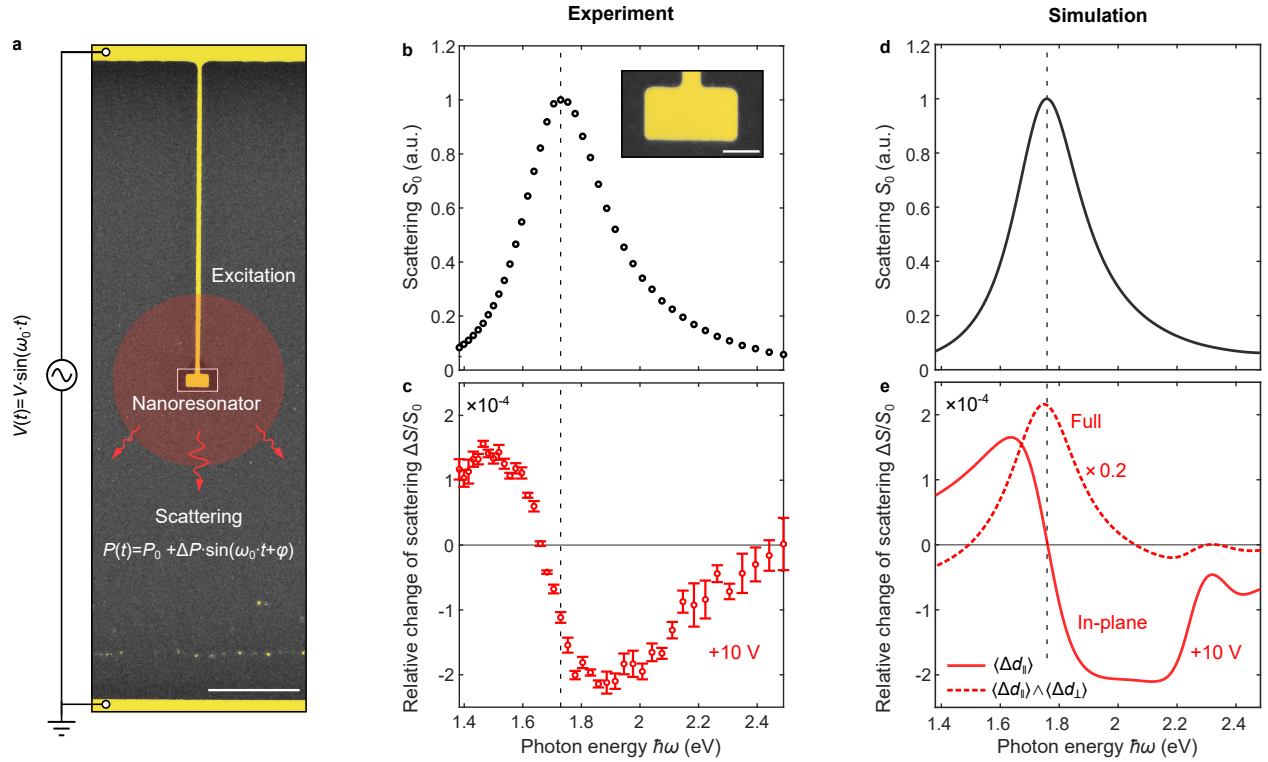


FIG. 3. **Measuring the voltage induced change of a plasmonic resonance.** **a**, Colored SEM image of a single electrically connected gold nanoresonator. The structure is driven with a sinusoidal voltage $V(t)$ while monitoring the scattered power $P(t)$. Scale bar is 500 nm. **b**, Measured scattering spectrum. The inset shows a colored close-up SEM image of the nanoresonator. Scale bar is 50 nm. **c**, Relative change of scattering as obtained from lock-in measurements for +10 V. **d**, Simulated scattering spectrum. **e**, Simulated relative change of scattering for +10 V by considering: only d_{\parallel} component perturbation depicted with red solid line, perturbation from both components depicted with dashed red line.

a purely classical term, exhibits a similar spectral shape (denoted as In-plane) as the experimental result, reaching a minimum value on the right slope of the resonance with a relative change of approximately -2×10^{-4} . The similarity to the experimental result is reflected in the obtained spectral shift of $\hbar\Delta\omega_r = (-25 \pm 2) \mu\text{eV}$. However, there is one crucial difference: the d_{\parallel} component perturbation has negligible imaginary part (see Fig. 2a) and therefore does not affect the loss of the system, as reflected in the obtained $\hbar\Delta\gamma_r$ value of $(0.7 \pm 0.1) \mu\text{eV}$. In contrast, when we include the d_{\perp} component perturbation obtained from DFT calculations, dominated by the large imaginary part (see Fig. 2a), we observe a maximum relative change of 1×10^{-3} at resonance (denoted as Full). This leads to a significant narrowing of the resonance for positive bias with a $\hbar\Delta\gamma_r$ value of $(-152.8 \pm 0.5) \mu\text{eV}$. Additionally, the spectral shift is reduced to $\hbar\Delta\omega_r = (-12 \pm 2) \mu\text{eV}$, since the real part of the perturbation coefficient for the d_{\perp} component has the same sign as the real part of the d_{\parallel} component. However, none of the d_{\perp} -component effects have been observed in experiment. Furthermore, to investigate the reproducibility and the spectral dependency of the perturbation we fabricate resonators with fixed width of 80 nm and height of 50 nm and vary the length in steps of 20 nm between 180 nm and 100 nm, with resonances covering the spectral range from

1.5 eV to 2 eV (see Supplementary Figure S9). In all instances we observe similar behaviour with smaller resonators exhibiting larger relative change.

V. DISCUSSION

The absence of the d_{\perp} -component effects, as calculated from DFT, suggests that contributions from the d_{\perp} component are effectively suppressed in the experiment. Assuming that the DFT jellium calculations – at least qualitatively – captures the surface electrodynamic phenomena of the real physical surface, this leads to the conclusion that either non-local effects counteract the perturbation as calculated with the LRA, or there is an anisotropy of the perturbed local permittivity with suppressed out-of-plane response. One possible explanation is that added electrons preferentially occupy surface states. This could also explain the observed decrease in loss with negative bias voltage, since surface states have larger carrier mobility as already observed in DC conductivity measurements [57, 58]. To further validate these assumptions, additional experiments are required that can clearly separate the contributions of nanoresonator's eigenfrequency change stemming from the perturbation of d_{\parallel} and d_{\perp} component. Fig. 2c

shows that perturbation strengths for all components are non-negligible, which can be attributed to the simplicity of the chosen geometry that does not have any pronounced geometrical features and large field enhancements. One possible way to disentangle the contributions stemming from d_{\parallel} and d_{\perp} , is by using a dimer antenna with a narrow gap [59]. Such a structure exhibits a large field enhancement in the gap in both the static and optical regimes, which according to Eq. (2), should enhance contributions from the d_{\perp} component. Nevertheless, if a dimer antenna possesses a symmetrical gap, applying a static field would result in the accumulation of charges with equal magnitude but opposite polarity on two sides of the gap. Consequently, this would give rise to anti-symmetric perturbations on the two sides of the gap, which in combination with a symmetrical optical field, would jeopardize our goal to observe the d_{\perp} component perturbation due to the anti-symmetric contributions that cancel each other as stated with Eq. (2). Therefore, to increase the effect of the d_{\perp} component, an antenna with a narrow and asymmetric gap should be chosen [56]. On the other hand, boosting contributions from the d_{\parallel} component is more challenging since the optical field enhancement is not as strong on the flanks of the structure and cannot be further enhanced by coupling effects as in the case of the d_{\perp} component. The only gain that a narrow gap could provide is that of the static field, implying the need for a globally asymmetric structure to overcome cancellation effects [60].

VI. CONCLUSION

We have presented both a theoretical and experimental investigation of charged plasmonic nanoresonators and their optical response. In our theoretical model we perturbed the Feibelman d -parameters in the LRA, which were calculated from the shape of the equilibrium and induced electron density at a charged jellium-air interface. We have demonstrated that the perturbation of the d_{\parallel} component exhibits a purely classical behavior, which is equivalent to a perturbation of the surface conductivity defined with bulk parameters. Moreover, it explains the observed spectral shift of the resonance frequency. However, the intriguing spectral narrowing of the resonance as more electrons are added to the resonator contradicts the behavior predicted by LRA calculations. We attribute this discrepancy to unaccounted non-classical effects such as: nonlocality and anisotropy of the local permittivity, which may result from the preferential occupation of surface states upon adding electrons to the structure. To provide stronger evidence for these claims, further modeling efforts beyond jellium considerations are required to calculate electrically induced perturbations of d -parameters, accounting for nonlocal effects and anisotropy. Additionally, as discussed in the text, exploring optimized geometries with stronger field localizations will help to better separate contributions stemming from the two d -parameters. Our findings pave the way for reducing losses in plasmonic resonators by gaining control over non-classical surface effects.

Methods

Numerical simulations. The perturbation of the optical response of a plasmonic nanoresonator under electrostatic biasing is numerically determined using the commercially available FEM solver (COMSOL Multiphysics 6.0) [61] for the electrodynamics. Our simulations involve a two-step process. Initially, we solve for the electrostatic field by applying a potential V to the structure using the AC/DC Module. This step allows us to obtain the induced surface electron density $\Delta n_0(\mathbf{r}_s, V)$. The ground potential is placed infinitely far away by employing an infinite element domain layer. In the second step, we conduct optical simulations using the wave optics module to analyze the scattering cross sections based on the local perturbation in the d -parameters influenced by the induced surface electron density. To introduce perturbations in the d -parameters, we employ mesoscopic boundary conditions (see Supplementary Section 1.6) implemented with an auxiliary potential method, as described in Ref. 20. The structure is excited with a plane wave polarized along the long axis of the nanoresonator, and the scattered light is collected at the bottom hemisphere to mimic the experimental setup. The optical permittivity of gold is taken from the experimental values for mono-crystalline gold provided by Olmon *et al.* [62], while glass is modeled using Sellmeier coefficients. For more information, please refer to Supplementary Section 1.3.

Sample fabrication. Mono-crystalline gold microplatelets, measuring 50 nm in thickness, are synthesized through a wet-chemical process outlined in Ref. 55. These microplatelets are then transferred onto a glass coverslip (24 mm \times 24 mm #1.5 Menzel) with evaporated metal layers featuring an array of electrode pads prepared by optical lithography and electron beam physical vapor deposition (20 nm chromium adhesion layer, 80 nm gold layer). The microplatelets are carefully positioned over the glass window on structured microscopic electrodes, ensuring a conductive connection between the flake and the metal film. Nanoresonator fabrication is conducted as described in Ref. 56.

Optical characterization. To capture dark-field scattering spectra of plasmonic nanoresonators, we employ an inverted optical microscope (TE2000-U, Nikon) equipped with a nanopositioning piezostage (NanoLPS200, Mad City Labs Inc.) and an oil-immersion microscope objective (PlanApochromat, 100 \times , NA = 1.45, Nikon). As excitation source, we utilize a supercontinuum laser (SuperK FIANIUM, FIR-20, NKT) that is spectrally shaped and scanned in 10 nm increments from 500 nm to 900 nm using an acousto-optic tunable filter (SuperK SELECT, NKT). The light from the laser is sent through a 300 μ m pinhole and focused to the back focal plane of the oil-immersion microscope objective via a 500 mm lens, providing a collimated beam at the sample. To separate the detection and excitation beam paths, a 50:50 beam splitter is employed. Light scattered by the structure above the critical angle and light reflected directly from the sample are separated using a circular beam block. Additionally, to minimize

potential stray light, an iris is positioned in the intermediate image plane and adjusted until the background is completely suppressed. The signal is collected using an optical power meter (1835-C, Newport). See also Supplementary Sections 2.1–2.3.

Electro-optical measurements. The nanoresonators are electrically connected to the macroscopic electrode pads using thin connector lines. They are then further connected via micro-manipulators to a function generator (DS 345, Stanford Research Instruments). An AC voltage is applied to the structure, and the scattered light, guided to the detector, is divided into two collecting channels using a 90:10 beam splitter. The majority of the light is captured by a silicon photodetector (DET36A2, Thorlabs) with a rise time of 14 ns, while the remaining portion is detected using an optical power meter (1835-C, Newport). The electrical signal from the photodetector is directed to a lock-in amplifier (DSP 7260, EG&G), with the reference signal obtained directly from the function generator output using a T-splitter. To enable the recording of correlated data, the entire process is monitored via a LabVIEW program. Throughout the measurements, the sample is continuously blow-dried using a laminar nitrogen stream.

Acknowledgments. T. F. acknowledges funding by the Volk-

swagen Foundation via an ‘Experiment!’ grant (95869), by the Marie Skłodowska-Curie Actions (MSCA) individual fellowship project PoSHGOAT (project- id 837928) and participation in CA19140 (FIT4NANO), supported by COST (European Cooperation in Science and Technology)

N. A. M. is a VILLUM Investigator supported by VILLUM FONDEN (Grant No. 16498). The Center for Polariton-driven Light–Matter Interactions (POLIMA) is funded by the Danish National Research Foundation (Project No. DNRF165).

Author contributions L. Z. conceived the idea and designed the experiment. J. M. fabricated the structures and performed the SEM measurements. R. K. and L. Z. built and optimized the electro-optical setup. L. Z. performed the electro-optical experiments. N. A. M. provided the derivation of the d -parameter perturbations. C. W. performed the DFT calculations. L. Z. conducted the FEM simulations. L. Z. analyzed the data and drafted the manuscript with input from all the authors. B. H. and T. F. supervised the project.

Correspondence and requests for materials should be addressed to L. Z. and T. F.

-
- [1] R. H. Ritchie. Plasma losses by fast electrons in thin films. *Physical Review*, 106(5):874, 1957.
- [2] P. Muhlschlegel, H.-J. Eisler, O. J. F. Martin, B. Hecht, and D. W. Pohl. Resonant optical antennas. *Science*, 308(5728):1607–1609, 2005.
- [3] L. Novotny. Effective wavelength scaling for optical antennas. *Physical Review Letters*, 98(26):266802, 2007.
- [4] A. G. Curto, G. Volpe, T. H. Taminiau, M. P. Kreuzer, R. Quidant, and N. F. van Hulst. Unidirectional emission of a quantum dot coupled to a nanoantenna. *Science*, 329(5994):930–933, 2010.
- [5] M. W. Knight, H. Sobhani, P. Nordlander, and N. J. Halas. Photodetection with active optical antennas. *Science*, 332(6030):702–704, 2011.
- [6] R. Zhang, Y. Zhang, Z. C. Dong, S. Jiang, C. Zhang, L. G. Chen, L. Zhang, Y. Liao, J. Aizpurua, Y. Luo, J. L. Yang, and J. G. Hou. Chemical mapping of a single molecule by plasmon-enhanced Raman scattering. *Nature*, 498(7452):82–86, 2013.
- [7] J. Kern, R. Kulllock, J. Prangsa, M. Emmerling, M. Kamp, and B. Hecht. Electrically driven optical antennas. *Nature Photonics*, 9(9):582–586, 2015.
- [8] M. Celebrano, X. Wu, M. Baselli, S. Großmann, P. Biagioni, A. Locatelli, C. De Angelis, G. Cerullo, R. Osellame, B. Hecht, et al. Mode matching in multiresonant plasmonic nanoantennas for enhanced second harmonic generation. *Nature Nanotechnology*, 10(5):412–417, 2015.
- [9] R. Chikkaraddy, B. de Nijs, F. Benz, S. J. Barrow, O. A. Scherman, E. Rosta, A. Demetriadou, P. Fox, O. Hess, and J. J. Baumberg. Single-molecule strong coupling at room temperature in plasmonic nanocavities. *Nature*, 535(7610):127–130, 2016.
- [10] P. J. Feibelman. Surface electromagnetic fields. *Progress in Surface Science*, 12(4):287–407, 1982.
- [11] U. Kreibig and L. Genzel. Optical absorption of small metallic particles. *Surface Science*, 156:678–700, 1985.
- [12] J. Tiggesbäumker, L. Köller, K.-H. Meiwes-Broer, and A. Liebsch. Blue shift of the mie plasma frequency in Ag clusters and particles. *Physical Review A*, 48(3):R1749, 1993.
- [13] E. Cottancin, G. Celep, J. Lermé, M. Pellarin, J. R. Huntzinger, J. L. Vialle, and M. Broyer. Optical properties of noble metal clusters as a function of the size: comparison between experiments and a semi-quantal theory. *Theoretical Chemistry Accounts*, 116(4-5):514–523, 2006.
- [14] J. Zuloaga, E. Prodan, and P. Nordlander. Quantum description of the plasmon resonances of a nanoparticle dimer. *Nano Letters*, 9(2):887–891, 2009.
- [15] K. J. Savage, M. M. Hawkeye, R. Esteban, A. G. Borisov, J. Aizpurua, and J. J. Baumberg. Revealing the quantum regime in tunnelling plasmonics. *Nature*, 491(7425):574–577, 2012.
- [16] J. A. Scholl, A. L. Koh, and J. A. Dionne. Quantum plasmon resonances of individual metallic nanoparticles. *Nature*, 483(7390):421–427, 2012.
- [17] C. Ciraci, R. T. Hill, J. J. Mock, Y. Urzhumov, A. I. Fernández-Domínguez, S. A. Maier, J. B. Pendry, A. Chilkoti, and D. R. Smith. Probing the ultimate limits of plasmonic enhancement. *Science*, 337(6098):1072–1074, 2012.
- [18] S. Raza, N. Stenger, S. Kadkhodazadeh, S. V. Fischer, N. Kostesha, A.-P. Jauho, A. Burrows, M. Wubs, and N. A. Mortensen. Blueshift of the surface plasmon resonance in silver nanoparticles studied with EELS. *Nanophotonics*, 2(2):131–138, 2013.
- [19] W. Zhu, R. Esteban, A. G. Borisov, J. J. Baumberg, P. Nordlander, H. J. Lezec, J. Aizpurua, and K. B. Crozier. Quantum

- mechanical effects in plasmonic structures with subnanometre gaps. *Nature Communications*, 7:11495, 2016.
- [20] Y. Yang, D. Zhu, W. Yan, A. Agarwal, M. Zheng, J. D. Joannopoulos, P. Lalanne, T. Christensen, K. K. Berggren, and M. Soljačić. A general theoretical and experimental framework for nanoscale electromagnetism. *Nature*, 576(7786):248–252, 2019.
- [21] S. Boroviks, Z.-H. Lin, V. A. Zenin, M. Ziegler, A. Dellith, P. A. D. Gonçalves, C. Wolff, S. I. Bozhevolnyi, J.-S. Huang, and N. A. Mortensen. Extremely confined gap plasmon modes: when nonlocality matters. *Nature Communications*, 13:3105, 2022.
- [22] N. A. Mortensen, P. A. D. Gonçalves, F. A. Shuklin, J. D. Cox, C. Tserkezis, M. Ichikawa, and C. Wolff. Surface-response functions obtained from equilibrium electron-density profiles. *Nanophotonics*, 10(14):3647–3657, 2021.
- [23] S. Raza, S. I. Bozhevolnyi, M. Wubs, and N. A. Mortensen. Nonlocal optical response in metallic nanostructures. *Journal of Physics: Condensed Matter*, 27(18):183204, 2015.
- [24] D. Jin, Q. Hu, D. Neuhauser, F. von Cube, Y. Yang, R. Sachan, T. S. Luk, D. C. Bell, and N. X. Fang. Quantum-spillover-enhanced surface-plasmonic absorption at the interface of silver and high-index dielectrics. *Physical Review Letters*, 115(19):193901, 2015.
- [25] J. B. Khurgin. Ultimate limit of field confinement by surface plasmon polaritons. *Faraday discussions*, 178:109–122, 2015.
- [26] T. V. Shahbazyan. Landau damping of surface plasmons in metal nanostructures. *Physical Review B*, 94(23):235431, 2016.
- [27] F. Wang, Y. Zhang, C. Tian, C. Girit, A. Zettl, M. Crommie, and Y. R. Shen. Gate-variable optical transitions in graphene. *Science*, 320(5873):206–209, 2008.
- [28] F. Bonaccorso, Z. Sun, T. Hasan, and A. C. Ferrari. Graphene photonics and optoelectronics. *Nature Photonics*, 4(9):611–622, 2010.
- [29] M. Liu, X. Yin, E. Ulin-Avila, B. Geng, T. Zentgraf, L. Ju, F. Wang, and X. Zhang. A graphene-based broadband optical modulator. *Nature*, 474(7349):64–67, 2011.
- [30] BG McMillan, LEA Berlouis, FR Cruickshank, and PF Brevet. Reflectance and electrolyte electroreflectance from gold nanorod arrays embedded in a porous alumina matrix. *Journal of Electroanalytical Chemistry*, 599(2):177–182, 2007.
- [31] P. Mulvaney, J. Pérez-Juste, M. Giersig, L. M. Liz-Marzán, and C. Pecharrmán. Drastic surface plasmon mode shifts in gold nanorods due to electron charging. *Plasmonics*, 1:61–66, 2006.
- [32] C. Novo, A. M. Funston, A. K. Gooding, and P. Mulvaney. Electrochemical charging of single gold nanorods. *Journal of the American Chemical Society*, 131(41):14664–14666, 2009.
- [33] T. Miyazaki, R. Hasegawa, H. Yamaguchi, H. Oh-oka, H. Nagato, I. Amemiya, and S. Uchikoga. Electrical control of plasmon resonance of gold nanoparticles using electrochemical oxidation. *The Journal of Physical Chemistry C*, 113(19):8484–8490, 2009.
- [34] T. A. Petach, M. Lee, R. C. Davis, A. Mehta, and D. Goldhaber-Gordon. Mechanism for the large conductance modulation in electrolyte-gated thin gold films. *Physical Review B*, 90(8):081108, 2014.
- [35] S. S. E. Collins, X. Wei, T. G. McKenzie, A. Funston, and P. C. Mulvaney. Single gold nanorod charge modulation in an ion gel device. *Nano Letters*, 16(11):6863–6869, 2016.
- [36] B. S. Hoener, H. Zhang, T. S. Heiderscheidt, S. R. Kirchner, A. S. De Silva Indrasekara, R. Baiyasi, Y. Cai, P. Nordlander, S. Link, C. F. Landes, and W.-S. Chang. Spectral response of plasmonic gold nanoparticles to capacitive charging: morphology effects. *The Journal of Physical Chemistry Letters*, 8(12):2681–2688, 2017.
- [37] T. Liu, M. Li, Y. Wang, Y. Fang, and W. Wang. Electrochemical impedance spectroscopy of single Au nanorods. *Chemical Science*, 9(19):4424–4429, 2018.
- [38] R. A. Maniyara, D. Rodrigo, R. Yu, J. Canet-Ferrer, D. S. Ghosh, R. Yongsunthon, D. E. Baker, A. Rezikyan, F. J. García de Abajo, and V. Pruneri. Tunable plasmons in ultrathin metal films. *Nature Photonics*, 13(5):328–333, 2019.
- [39] C. F. Bohren and A. J. Hunt. Scattering of electromagnetic waves by a charged sphere. *Canadian Journal of Physics*, 55(21):1930–1935, 1977.
- [40] M. Zapata Herrera, J. Aizpurua, A. K. Kazansky, and A. G. Borisov. Plasmon response and electron dynamics in charged metallic nanoparticles. *Langmuir*, 32(11):2829–2840, 2016.
- [41] W. Li, Q. Zhou, P. Zhang, and X.-W. Chen. Direct electro plasmonic and optic modulation via a nanoscopic electron reservoir. *Physical Review Letters*, 128(21):217401, 2022.
- [42] M. T. Sheldon, J. van de Groep, A. M. Brown, A. Polman, and H. A. Atwater. Plasmoelectric potentials in metal nanostructures. *Science*, 346(6211):828–831, 2014.
- [43] N. Jiang, X. Zhuo, and J. Wang. Active plasmonics: principles, structures, and applications. *Chemical Reviews*, 118(6):3054–3099, 2017.
- [44] M. Weber and A. Liebsch. Density-functional approach to second-harmonic generation at metal surfaces. *Physical Review B*, 35(14):7411, 1987.
- [45] M. Khalid and C. Ciraci. Enhancing second-harmonic generation with electron spill-out at metallic surfaces. *Communications Physics*, 3:214, 2020.
- [46] A. Noor, M. Khalid, F. De Luca, H. M. Baghrmian, M. Castritto, A. D’Orazio, and C. Ciraci. Second-harmonic generation in plasmonic waveguides with nonlocal response and electron spill-out. *Physical Review B*, 106(4):045415, 2022.
- [47] T. Takeuchi and K. Yabana. Electron spill-out effect on third-order optical nonlinearity of metallic nanostructure. *Physical Review A*, 106(6):063517, 2022.
- [48] A. Varas, P. García-González, J. Feist, F. J. García-Vidal, and A. Rubio. Quantum plasmonics: from jellium models to ab initio calculations. *Nanophotonics*, 5(3):409–426, 2016.
- [49] N. A. Mortensen. Mesoscopic electrostatics at metal surfaces. *Nanophotonics*, 10(10):2563–2616, 2021.
- [50] A. Rodríguez Echarri, P. A. D. Gonçalves, C. Tserkezis, F. J. García de Abajo, N. A. Mortensen, and J. D. Cox. Optical response of noble metal nanostructures: quantum surface effects in crystallographic facets. *Optica*, 8(5):710–721, 2021.
- [51] T. Christensen, W. Yan, A.-P. Jauho, M. Soljačić, and N. A. Mortensen. Quantum corrections in nanoplasmonics: shape, scale, and material. *Physical Review Letters*, 118(15):157402, 2017.
- [52] P. Lalanne, W. Yan, K. Vynck, C. Sauvan, and J.-P. Hugonin. Light interaction with photonic and plasmonic resonances. *Laser & Photonics Reviews*, 12(5):1700113, 2018.
- [53] J. Yang, H. Giessen, and P. Lalanne. Simple analytical expression for the peak-frequency shifts of plasmonic resonances for sensing. *Nano Letters*, 15(5):3439–3444, 2015.
- [54] W. Yan, M. Wubs, and N. A. Mortensen. Projected dipole model for quantum plasmonics. *Physical Review Letters*, 115(13):137403, 2015.
- [55] E. Krauss, R. Kulklock, X. Wu, P. Geisler, N. Lundt, M. Kamp, and B. Hecht. Controlled growth of high-aspect-ratio single-crystalline gold platelets. *Crystal Growth & Design*, 18(3):1297–1302, 2018.
- [56] J. Meier, L. Zurak, A. Locatelli, T. Feichtner, R. Kulklock, and B. Hecht. Controlling field asymmetry in nanoscale gaps for

second harmonic generation. *arXiv:2210.14105*.

- [57] G. Bonfiglioli, E. Coen, and R. Malvano. Modulation of conductivity by surface charges in metals. *Physical Review*, 101(4):1281, 1956.
- [58] G. Bonfiglioli and R. Malvano. Surface states in metals. *Physical Review*, 115(2):330, 1959.
- [59] J. C. Prangma, J. Kern, A. G. Knapp, S. Grossmann, M. Emmerling, M. Kamp, and B. Hecht. Electrically connected resonant optical antennas. *Nano Letters*, 12(8):3915–3919, 2012.
- [60] P. Grimm, S. Zeißner, M. Rödel, S. Wiegand, S. Hammer, M. Emmerling, E. Schatz, R. Kulloock, J. Pflaum, and B. Hecht. Color-switchable subwavelength organic light-emitting antennas. *Nano Letters*, 22(3):1032–1038, 2022.
- [61] COMSOL Multiphysics v. 6.0. www.comsol.com. COMSOL AB, Stockholm, Sweden.
- [62] R. L. Olmon, B. Slovick, T. W. Johnson, D. Shelton, S.-H. Oh, G. D. Boreman, and M. B. Raschke. Optical dielectric function of gold. *Physical Review B*, 86(23):235147, 2012.

Supplementary material

Direct electrical modulation of surface response in a single plasmonic nanoresonator

Luka Zurak¹, Christian Wolff², Jessica Meier¹, René Kullo¹, N. Asger Mortensen^{2,3}, Bert Hecht¹, and Thorsten Feichtner¹

¹Nano-Optics and Biophotonics Group, Experimental Physics 5, Institute of Physics, University of Würzburg, Germany

²POLIMA - Center for Polariton-driven Light-Matter Interactions, University of Southern Denmark, Campusvej 55, DK-5230 Odense M, Denmark

³Danish Institute for Advanced Study, University of Southern Denmark, Campusvej 55, DK-5230 Odense M, Denmark

July 4, 2023

Contents

1	1 Model	2
2	1.1 Lossy harmonic oscillator	2
3	1.2 Classical models	2
4	1.3 Nanoresonator on a substrate	3
5	1.4 Feibelman d -parameters	5
6	1.5 Evaluating the d -parameters	6
7	1.6 Mesoscopic boundary conditions	7
8	1.7 Surface-response functions and classical models	8
9	1.8 Effect of the d -parameters on the properties of plasmonic resonance	8
10	2 Experiment	10
11	2.1 Electro-optical setup	10
12	2.2 Scattering measurements	10
13	2.3 Characteristics of the excitation source	11
14	2.4 Exemplary lock-in measurements	13
15	2.5 Changing the length of the nanoresonator	13

1 Model

1.1 Lossy harmonic oscillator

In classical terms, a lossy harmonic oscillator's resonance line shape can be described by a Lorentzian function $L(\omega; \omega_r, \gamma_r)$ with resonance position ω_r and width γ_r (see Fig. 1a in the main text). It is straightforward to show that a small perturbation of the resonance frequency $\Delta\omega_r$, produces a distinct line shape of the relative change of resonance as shown in Fig. 1b in the main text. This can be expressed analytically as

$$\frac{\Delta L_{\omega_r}}{L_0} \simeq \frac{1}{L_0} \frac{\partial L}{\partial \omega_r} \Delta\omega_r = 2L_0(\omega - \omega_{r0})\Delta\omega_r, \quad (\text{S1.1})$$

where $\Delta L_{\omega_r} \equiv L(\omega; \omega_{r0} + \Delta\omega_r, \gamma_{r0}) - L(\omega; \omega_{r0}, \gamma_{r0})$ and $L_0 \equiv L(\omega; \omega_{r0}, \gamma_{r0})$ is the unperturbed resonance, with resonance position ω_{r0} and width γ_{r0} . Extrema of the relative change curve are reached at frequencies $\omega_{\pm} = \omega_{r0} \pm \gamma_{r0}/2$, where the relative change of the resonance is

$$\left. \frac{\Delta L_{\omega_r}}{L_0} \right|_{\omega=\omega_{\pm}} = \pm 2Q \frac{\Delta\omega_r}{\omega_{r0}}. \quad (\text{S1.2})$$

Here, $Q = \omega_r/\gamma_r$ stands for the quality factor of the resonance. In the case of a blue-shifted resonance ($\Delta\omega_r > 0$), the relative change reaches its maximum on the blue side of the resonance and a minimum on the red side (see Fig. 1b in the main text). Conversely, for a red-shifted resonance ($\Delta\omega_r < 0$), we expect to observe the opposite pattern. Additionally, the change in the resonance position can be determined by examining the slope of the relative change curve at the resonance frequency (see Fig. 1b in the main text):

$$\left. \frac{\partial}{\partial \omega} \frac{\Delta L_{\omega_r}}{L_0} \right|_{\omega=\omega_{r0}} = \frac{8Q}{\gamma_{r0}} \frac{\Delta\omega_r}{\omega_{r0}}. \quad (\text{S1.3})$$

A small perturbation of the resonance width $\Delta\gamma_r$, will also lead to a characteristic line shape of the relative change curve, given by the expression:

$$\frac{\Delta L_{\gamma_r}}{L_0} \simeq \frac{1}{L_0} \frac{\partial L}{\partial \gamma_r} \Delta\gamma_r = -L_0 \frac{\gamma_{r0}}{2} \Delta\gamma_r, \quad (\text{S1.4})$$

where $\Delta L_{\gamma_r} \equiv L(\omega; \omega_{r0}, \gamma_{r0} + \Delta\gamma_r) - L(\omega; \omega_{r0}, \gamma_{r0})$. Thus, the relative change of line shape follows the shape of the resonance, and an extremum is reached at the resonance frequency ω_{r0} , with a value of:

$$\left. \frac{\Delta L_{\gamma_r}}{L_0} \right|_{\omega=\omega_{r0}} = -2 \frac{\Delta\gamma_r}{\gamma_{r0}}, \quad (\text{S1.5})$$

where an increase/decrease in damping leads to an increase/decrease in resonance width and therefore to a negative/positive relative change.

1.2 Classical models

When discussing the optical response of charged plasmonic nanoresonators, two classical models are relevant. These models assume that the excess charge arises from a variation in the number of free electrons N_0 .

Bulk model

In a simplified yet illustrative scenario, an excess charge is uniformly distributed throughout the volume V of the resonator – one should note that this assumption is obviously incorrect and misleading. Despite its flaws, this model is quite commonly employed to provide a rough estimate of the magnitude of the induced change. Consequently, this distribution induces changes in the material properties of the resonator by altering its bulk conductivity. The conductivity is given with the equation [1]:

$$\sigma_b = i\varepsilon_0 \frac{\omega_p^2}{\omega + i\gamma}, \quad (\text{S1.6})$$

58 where $\omega_p \propto \sqrt{n_0}$ is the plasma frequency and $n_0 = N_0/V$ is the free electron density. It can be shown that the
 59 resonance frequency of the system is proportional to the plasma frequency of the system. Therefore, changing
 60 the density of the free electrons effectively causes a change in the resonance frequency.

61 Surface model

62 Bohren and Hunt introduced the surface current model [2]. In this model, the excess charge induces a change
 63 in the surface electron density η_0 , resulting in a modification of the surface conductivity σ_s . By applying the
 64 Drude model to the thin surface charge layer consisting of electrons with mass m and charge q_e , the surface
 65 conductivity can be expressed using the following equation:

$$\sigma_s = i \frac{q_e^2}{m} \frac{\eta_0}{\omega + i\gamma}, \quad (\text{S1.7})$$

66 where γ is the collision rate at the surface. When the surface conductivity is perturbed, it induces a modification
 67 in the surface current $\mathbf{K} = \sigma_s \mathbf{E}_{\parallel}$, where \mathbf{E}_{\parallel} is the tangential component of the electric field at the surface. To
 68 incorporate the presence of the surface current in Maxwell's equations, the boundary condition for the tangential
 69 component of the magnetic field \mathbf{H} needs to be redefined as

$$\Delta \mathbf{H}_{\parallel} = \mathbf{K} \times \hat{x}_{\perp}, \quad (\text{S1.8})$$

70 where \hat{x}_{\perp} is normal unit vector pointing away from material 1 to material 2 and $\Delta \mathbf{H} = (\mathbf{H}_2 - \mathbf{H}_1)$. The
 71 implications of the surface model, regarding its influence on the resonance, are not as clear as those in the case
 72 of the bulk model. However, a direct comparison can be made when discussing the special case of a sphere [2].
 73 There, as in the case of the bulk model, it can be shown that introducing a change to the number of free electrons
 74 influences the resonance frequency.

75 1.3 Nanoresonator on a substrate

76 When dealing with a realistic geometry, such as a rectangular nanoresonator on a glass substrate (as depicted
 77 in Fig. S1a), the distribution of the induced surface charge $\Delta\eta_0(\mathbf{r}_s, V)$ is not uniform. In order to determine the
 78 response of such a system, we utilize finite element method (FEM) simulations and solve Maxwell's equations
 79 in a two-step procedure using commercially available numerical solver COMSOL Multiphysics. In the initial
 80 step, we solve for the static electric field and the induced surface charge density. Subsequently, we conduct
 81 simulations at optical frequencies. The simulation geometry consists of a sphere with a radius r_{sur} of 400 nm
 82 and a layer with a thickness t_a of 200 nm. This layer serves as the infinite element domain (IED) for electro-
 83 static simulations and the perfectly matched layer (PML) for optical simulations. In Fig. S1b, we present the
 84 geometry of the nanoresonator, which closely resembles the structures realized in the experimental setup. The
 85 nanoresonator's dimensions are as follows: length (l) = 140 nm, width (w) = 80 nm, and height (h) = 50 nm.
 86 Due to employed fabrication procedure, it is surrounded by a trench with a depth (t_d) of 40 nm and a width (t_w)
 87 of 50 nm (similar to Ref. [3]). Consequently, it stands atop a glass pedestal with a total height (p) of 50 nm. The
 88 single resonator exhibits a dipolar mode, as evidenced by the simulated radiation pattern (see inset of Fig. S1c).
 89 The peak position occurs around 1.7 eV, and the FWHM is roughly 280 meV. As in the experiment we solely
 90 observe light scattered above the critical angle, we conducted calculations to confirm that the shape of the res-
 91 onance remains unaffected by the measurement procedure. To this end we compared the scattered power above
 92 the critical angle to the total scattered power (see Fig. S1c).

93 In the case of electrostatic simulations, the surface of the nanoresonator is assumed to be an equipotential,
 94 with an electric potential V , while a reference potential V_{ref} (ground) is positioned at an infinitely far distance
 95 by employing the IED. The dielectric constant of the glass κ_{glass} is set to 5, which falls within the typical range
 96 for glasses (from 5 to 10). This enhances the capacitance at the interface between gold and glass. At the corners
 97 of the nanoresonator, the static electric field reaches values of 0.35 GV/m, while the average induced surface
 98 charge density amounts to 2.7 mC/m². By integrating the induced charge density over the nanoresonator's sur-
 99 face for an applied potential of 10 V, the total induced charge is approximately 0.1 fC. This charge is equivalent
 100 to removing approximately 700 electrons from the nanoresonator's surface, resulting in a total self-capacitance
 101 of the system of around 10 aF. For our optical simulations, we use the Olmon SC material data for gold, which
 102 we fit using a plasma frequency of $\hbar\omega_p = 8.3$ eV and collision time of $\tau = 14$ fs. The considered spectral range

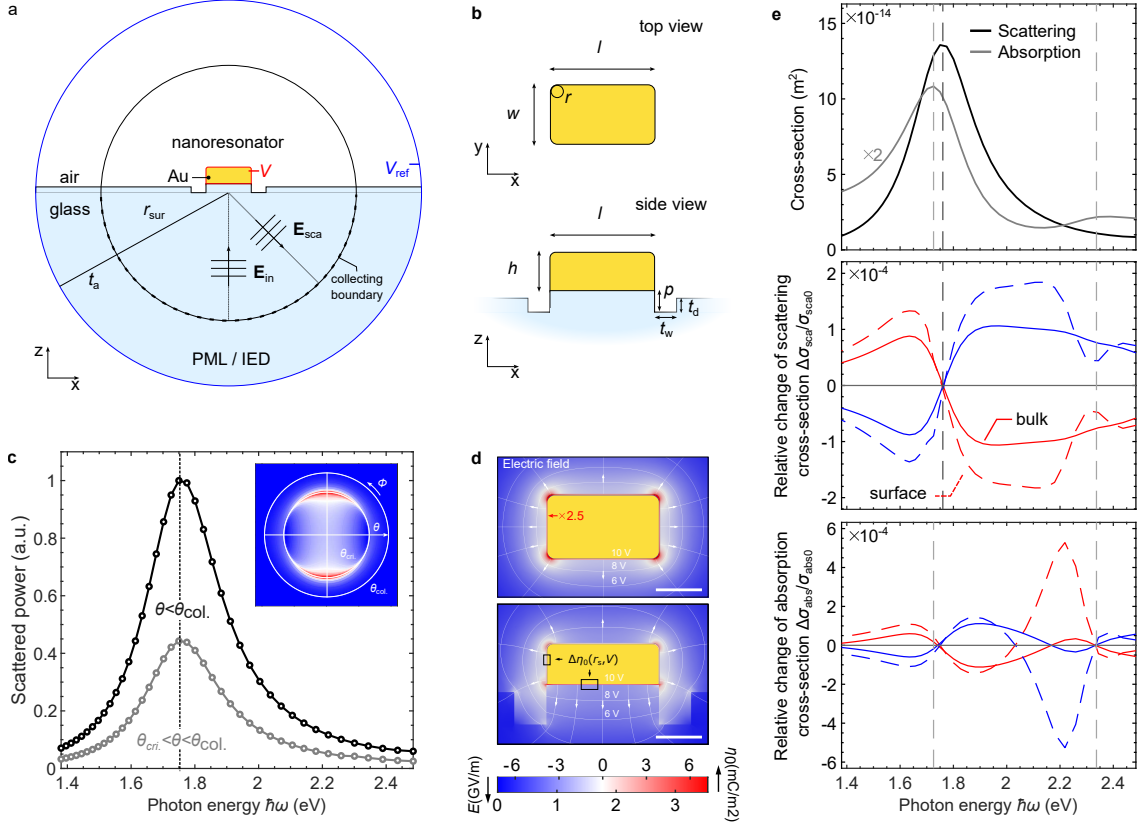


FIG. S1: **Electrically charged nanoresonator on a glass substrate.** **a**, The side view of the complete simulation geometry. In the electrostatic simulations, surface of the structure is an equipotential on a potential V , while the reference potential V_{ref} , situated on the outer surface of the IED, is set to zero volts. The structure is excited from below at a zero angle, using a plane wave characterized by the electric field \mathbf{E}_{in} . The light scattered by the structure is carried by the scattered electric field \mathbf{E}_{sca} , collected at the bottom hemisphere. **b**, Geometry of the nanoresonator. **c**, The simulated scattering spectra are obtained by integrating the scattered power over specific regions of the hemisphere through radiation pattern calculations. The inset illustrates a radiation pattern. **d**, Results of electrostatic simulations. Electrostatic field and induced surface electron density. **e**, (top) The absorption and scattering cross-section are presented. (middle) The relative change of the scattering cross-section. (bottom) The relative change in absorption cross-section.

103 spans from 0.5 eV (2500 nm) to 1.24 eV (1000 nm), where the free electron response dominates. Due to the
104 dependence of the plasma frequency on both the free electron density and effective mass, it is not possible to
105 obtain the exact value for the unperturbed bulk density n_0 of the system. However, assuming that the effective
106 mass of the electron is equal to the rest mass of an electron $m = m_e$, the unperturbed free electron density is
107 $n_0 \approx 5 \cdot 10^{28} \text{ m}^{-3}$. To examine the impact of the additional electrons, we apply both the surface and the bulk
108 model. In the surface model, we introduce a surface current \mathbf{K} , with conductivity determined from Eq. (S1.5).
109 This model is implemented in the numerical solver through the application of built-in boundary conditions for
110 the tangential component of the magnetic field, as stated with Eq. (S1.8). The results for both models are il-
111 lustrated in Fig. S1e. We observe a similar behavior in the relative change of scattering for both the bulk and
112 the surface model, reaching values of approximately 1×10^{-4} on the resonance slopes, with no alteration in
113 the resonance frequency. This pattern of the relative change is characteristic of a resonance-induced shifts (see
114 Fig. 1a in the main text). Although the most significant change occurs near the resonance frequency, there are
115 additional undulations in the relative change at around 2.3 eV. These changes are attributed to the presence of
116 a dark mode, which is not clearly discernible in the scattering cross-section but is observable in the absorption
117 cross-section.

1.4 Feibelman d -parameters

In classical electrodynamics, an interface between a metal and a dielectric is considered to be infinitesimally thin, suggesting that the induced charge density $\rho(x_\perp)$ is strictly confined to the interface, meaning $\rho(x_\perp) \propto \delta(x_\perp)$ [4], where $\delta(x_\perp)$ is a delta function. However, in his seminal work [5] Feibelman demonstrated that the first-order correction to the multipole expansion of induced charge density introduces two additional quantities known as “ d -parameters”. The d -parameters, denoted as $d_\perp \equiv d_\perp(\omega)$ and $d_\parallel \equiv d_\parallel(\omega)$, are frequency-dependent centroids of the induced charge density, and of the normal derivative of the tangential current $\mathbf{J}_\parallel(x_\perp)$, respectively (see [4]). That is, we can express them with the following equations

$$\begin{aligned} d_\perp &= \frac{\int_{-\infty}^{\infty} x_\perp \rho(x_\perp) dx_\perp}{\int_{-\infty}^{\infty} \rho(x_\perp) dx_\perp}, \\ d_\parallel &= \frac{\int_{-\infty}^{\infty} x_\perp \frac{\partial}{\partial x_\perp} J_\parallel(x_\perp) dx_\perp}{\int_{-\infty}^{\infty} \frac{\partial}{\partial x_\perp} J_\parallel(x_\perp) dx_\perp}. \end{aligned} \quad (\text{S1.9})$$

The d -parameters serve as descriptors of the optical properties of realistic metal-dielectric interfaces, similar to how permittivity characterizes the bulk properties. They provide information about the non-locality and inhomogeneous nature of the medium in proximity of the interface. Consequently, they are an appropriate tool for investigating the impact of electrostatically induced surface charge on the optical properties of plasmonic nanoresonators.

Typically, the d -parameters are obtained through ab-initio calculations that examine the response of metal surfaces to time-varying electric fields. For example, time-dependent density-functional theory (TDDFT) is commonly employed for this purpose [6, 7]. In certain cases, analytical evaluations of the response can be performed, such as through semiclassical hydrodynamic models [8, 9, 10]. However, in all instances, the approach to retrieve the d -parameters has been to assess the non-equilibrium electron response and employ Eq. (S1.9).

A recent study [11] has revealed that even when considering the spill-out effect and employing the local-response approximation, there remains a finite contribution to the metallic surface-response functions. The contribution arising from spill-out effects can be obtained by considering the equilibrium electron density, assuming a smooth transition from its bulk value deep within the metal to zero outside. Calculating these contributions involves evaluating the following expressions

$$d_\perp = \frac{1}{\varepsilon_m^{-1} - \varepsilon_d^{-1}} \int_{-\infty}^{\infty} dx_\perp [\varepsilon_{\text{LRA}}^{-1}(x_\perp) - \varepsilon_{\text{PCA}}^{-1}(x_\perp)], \quad (\text{S1.10a})$$

$$d_\parallel = \frac{1}{\varepsilon_m - \varepsilon_d} \int_{-\infty}^{\infty} dx_\perp [\varepsilon_{\text{LRA}}(x_\perp) - \varepsilon_{\text{PCA}}(x_\perp)], \quad (\text{S1.10b})$$

which incorporate the dielectric function of the surrounding materials $\varepsilon_m, \varepsilon_d$ and its profile near the interface. Here, $\varepsilon_{\text{LRA}}(x_\perp)$ is smoothly varying dielectric function governed by the electron spill-out (as described with Eq. (4) in the main text), while $\varepsilon_{\text{PCA}}(x_\perp)$ is a piecewise-constant dielectric function. Since the dielectric function in the local-response approximation depends on the equilibrium electron density, for an applied voltage V the electron density will be perturbed at the interface with the surrounding dielectric material, resulting in a new equilibrium electron density $n_0(x_\perp, V) = n_0(x_\perp) + \Delta n_0(x_\perp, V)$. Consequently, this leads to the perturbation of the local dielectric function $\varepsilon_{\text{LRA}}(x_\perp, V) = \varepsilon_{\text{LRA}}(x_\perp) + \Delta \varepsilon_{\text{LRA}}(x_\perp, V)$. To inspect the influence of the applied voltage on the d -parameters (see Eq. (3) in the main text) we need to calculate the partial derivatives of the expressions given with Eq. (S1.10a), and (S1.10b):

$$\frac{\partial d_\perp}{\partial V} = \frac{1}{\varepsilon_m^{-1} - \varepsilon_d^{-1}} \int_{-\infty}^{\infty} dx_\perp \frac{\partial}{\partial V} \varepsilon_{\text{LRA}}^{-1}(x_\perp, V), \quad (\text{S1.11})$$

$$\frac{\partial d_\parallel}{\partial V} = \frac{1}{\varepsilon_m - \varepsilon_d} \int_{-\infty}^{\infty} dx_\perp \frac{\partial}{\partial V} \varepsilon_{\text{LRA}}(x_\perp, V). \quad (\text{S1.12})$$

151 From here Eq. (5a) and Eq. (5b) in the main text follow immediately.

152 In the main text, we have already discussed the evaluation of Eq. (5b) for the d_{\parallel} component, which does not
 153 depend on the shape of either the equilibrium or induced electron density. However, the calculation of the per-
 154 turbation coefficient for the d_{\perp} component involves some additional complexity, as the integral within Eq. (5a)
 155 in the main text relies on the inverse square of the local permittivity. This necessitates precise knowledge of the
 156 local electron response in the out-of-plane direction at the metal-dielectric interface. Since the induced change
 157 in the permittivity, $\Delta\epsilon_{\text{LRA}}(x_{\perp}, V)$, is considerably smaller than the unperturbed permittivity, $\epsilon_{\text{LRA}}(x_{\perp}, 0)$, we
 158 can simplify the expression (refer to Eq. (5a) in the main text) to

$$\begin{aligned} \frac{\partial d_{\perp}}{\partial V} &\approx \frac{\epsilon_d \epsilon_m}{\epsilon_m - \epsilon_d} \int_{-\infty}^{\infty} dx_{\perp} \frac{1}{\epsilon_{\text{LRA}}^2(x_{\perp})} \frac{\partial}{\partial V} \epsilon_{\text{LRA}}(x_{\perp}, V) \\ &= \frac{\epsilon_d \epsilon_m}{\epsilon_d - \epsilon_m} \frac{\omega_p^2}{\omega^2 + i\gamma\omega} \frac{1}{n_0} \int_{-\infty}^{\infty} dx_{\perp} \frac{1}{\epsilon_{\text{LRA}}^2(x_{\perp})} \frac{\partial \Delta n_0(x_{\perp}, V)}{\partial V}. \end{aligned} \quad (\text{S1.13})$$

159 Therefore, using Eq. (7) from the main text, we can express the d_{\perp} perturbation coefficient as

$$\frac{\partial d_{\perp}(\mathbf{r}_s, V)}{\partial V} \approx \frac{\epsilon_d \epsilon_m}{\epsilon_d - \epsilon_m} \frac{\omega_p^2}{\omega^2 + i\gamma\omega} \frac{C_s(\mathbf{r}_s)}{q_e} \frac{1}{n_0} \int_{-\infty}^{\infty} dx_{\perp} \frac{p(x_{\perp})}{\epsilon_{\text{LRA}}^2(x_{\perp})}. \quad (\text{S1.14})$$

160 Spatial dependency \mathbf{r}_s has been reinstated through the local surface capacitance $C_s(\mathbf{r}_s)$.

161 1.5 Evaluating the d -parameters

162 Equation (S1.14) involves an integral where the integrand depends on the inverse square of the local permittivity
 163 and the shape of the induced electron density. In order to address this, we conduct Density Functional Theory
 164 (DFT) calculations using the "Jellium" approximation, which allows us to obtain electron densities as depicted
 165 in Fig. S2a. Specifically, we present the results for the case of $r_s = 3.18$ corresponding to bulk electron density
 166 of $n_0 \approx 5 \cdot 10^{28} \text{m}^{-3}$, as determined from a Drude model fit to the material data as discussed in SI section 1.3.
 167 To evaluate the integral, it is necessary to choose a spatially varying background permittivity $\epsilon_b(x_{\perp})$. Deep
 168 inside the metal, it corresponds to the interband transitions contribution, $\epsilon_{\text{bm}} = \epsilon_m - \epsilon_{\text{D}}$, where ϵ_{D} represents
 169 the Drude free-electron contribution. In the dielectric, it corresponds to the material permittivity ϵ_d . We adopt
 170 a smooth function that connects these two contributions, following the equilibrium electron density

$$\epsilon_b(x_{\perp}) = n_0(x_{\perp}) \cdot \epsilon_{\text{bm}} + (1 - n_0(x_{\perp})) \cdot \epsilon_d. \quad (\text{S1.15})$$

171 Consequently, we obtain a smooth local permittivity ϵ_{LRA} , which is illustrated in Fig. S2b. The plot demon-
 172 strates a gradual transition from the permittivity of the metal to that of the dielectric. Due to the metal's
 173 significantly negative real part of permittivity and a small positive real permittivity of the dielectric, there exists
 174 a location where the real part of the local permittivity crosses zero. This specific region is denoted with a black
 175 rectangle in Fig. S2b and holds significance for the integral evaluation since the integrand contains the inverse
 176 square of the local permittivity, $\epsilon_{\text{LRA}}^{-2}$, which we can restate as follows:

$$\frac{1}{\epsilon_{\text{LRA}}^2} = \frac{(\epsilon_{\text{LRA}}^*)^2}{|\epsilon_{\text{LRA}}|^4}. \quad (\text{S1.16})$$

177 In Fig. S2c we present a zoomed-in view of the real and imaginary part of the local permittivity in the vicinity
 178 where epsilon approaches zero. Additionally, we show the absolute value $|\epsilon_{\text{LRA}}|$ in Fig. S2d. It is evident that
 179 the absolute value of local permittivity exhibits an asymmetry with respect to the position of the minimum,
 180 denoted as $x_{\perp 0}$. Specifically, the values on the left side ($x_{\perp} < x_{\perp 0}$) are slightly larger than the values at
 181 equidistant locations on the right side ($x_{\perp} > x_{\perp 0}$). As a result, $|\epsilon_{\text{LRA}}|^{-4}$ will exhibit a contrasting asymmetry,
 182 enhancing contributions from the right side of the peak position. Consequently, both the real and imaginary
 183 parts of the integrand, $\epsilon_{\text{LRA}}^{-2}$, will exhibit the same asymmetry, as depicted in Fig. S2e. We determine the
 184 perturbation coefficient for the gold-glass interface and present it in Fig. S2 f. In the inset of the figure, we

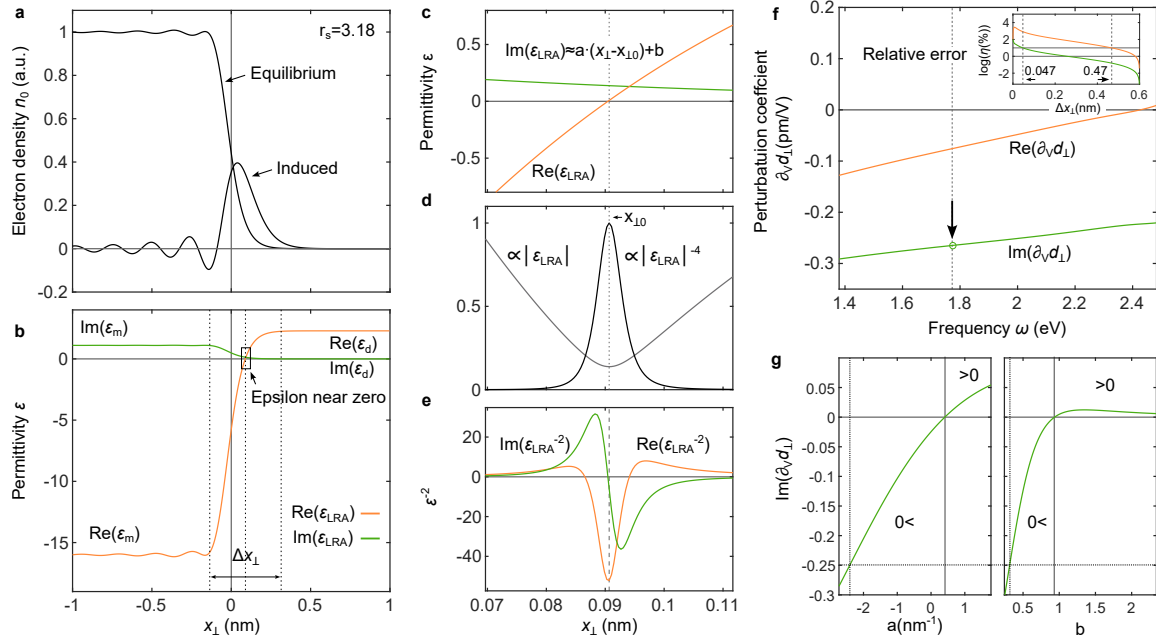


FIG. S2: **Evaluating the d_{\perp} perturbation coefficient.** **a**, Equilibrium and induced electron density for $r_s = 3.18$. **b**, Spatial dependency of local permittivity on gold-glass interface. **c**, Zoom-in region where local permittivity approaches zero denoted with black rectangle in **a**. **d**, Plot of absolute value of local permittivity and inverse of fourth power in epsilon near zero region. **e**, Real and imaginary part of square of inverse local permittivity in epsilon near zero region. **f**, Surface averaged perturbation coefficient of the d_{\perp} component. **f**, Influence of the imaginary part of local permittivity represented with line on the imaginary part of the perturbation coefficient with change introduced to line slope (left) and line y-intercept (right).

185 provide a logarithmic plot of the relative error η , showcasing the dependence of the real and imaginary parts
 186 of the perturbation coefficient on the size of the integration interval Δx_{\perp} (illustrated in Fig. S2a), centered
 187 around the location of minimum $x_{\perp 0}$. It is apparent that in order to accurately determine the real value with
 188 a relative error of 10% or less, a relatively large integration interval, larger than 0.5 nm is required. On the
 189 other hand, the same error for the imaginary part can be achieved with an integration interval of approximately
 190 $\Delta x_{\perp} \approx 0.05$ nm. Therefore, the shape of the local permittivity within a relatively small spatial interval plays a
 191 crucial role in determining the imaginary part of the perturbation coefficient. To investigate this influence, we
 192 maintain the real part of the permittivity $\text{Re}(\epsilon_{\text{LRA}})$ as given by the model and assume that the imaginary part can
 193 be approximated by a linear equation, $\text{Im}(\epsilon_{\text{LRA}}) \approx a(x_{\perp} - x_{\perp m}) + b$. In Fig. S2g, we illustrate the impact of the
 194 line slope, a (left), and the y-intercept, b (right), on the imaginary part of the perturbation coefficient. It can be
 195 observed that by increasing the line slope in a positive manner, the perturbation coefficient can be enhanced and
 196 rendered positive for $a > 0.3 \text{ nm}^{-1}$. Similarly, a positive perturbation coefficient can be achieved by increasing
 197 the y-intercept past the value of 0.9. This can be understood as introducing a change in asymmetry to the
 198 absolute value of local permittivity which is then translated to real and imaginary part of the inverse square of
 199 the permittivity.

200 1.6 Mesoscopic boundary conditions

201 As exemplified by Yang, Zhu and others [12], the d -parameters can be introduced into classical equations by
 202 means of boundary conditions, as they govern the surface polarization given with Eq. (1) in the main text. When
 203 incorporating this additional surface polarization at the interface between two materials, the revised boundary

204 conditions are as follows:

$$\Delta D_{\perp} = -i\omega^{-1}\nabla_{\parallel} \cdot \mathbf{K} = -d_{\perp}\nabla_{\parallel}E_{\perp} \quad (\text{S1.17a})$$

$$\Delta B_{\perp} = 0 \quad (\text{S1.17b})$$

$$\Delta \mathbf{E}_{\parallel} = -\frac{1}{\varepsilon_0}\nabla_{\parallel}\pi = -d_{\perp}\nabla_{\parallel}E_{\perp} \quad (\text{S1.17c})$$

$$\Delta \mathbf{H}_{\parallel} = \mathbf{K} \times \mathbf{n} = i\omega d_{\parallel}\Delta \mathbf{D}_{\parallel} \times \mathbf{n} \quad (\text{S1.17d})$$

205 Boundary conditions are implemented in FEM simulations using the auxiliary field method as discussed in
206 Ref. [12].

207 1.7 Surface-response functions and classical models

208 If we make the assumption that the perturbation caused by d_{\perp} component on the parallel component of the
209 electric field is negligible (from Eq. (S1.17c) $\Delta \mathbf{E}_{\parallel} \approx \mathbf{0}$), then we can approximate $\Delta \mathbf{D}_{\parallel}$ as $\varepsilon_0(\varepsilon_d - \varepsilon_m)\mathbf{E}_{\parallel}$.
210 Consequently, the expression for the perturbation of the surface current is

$$\Delta \mathbf{K} = i\omega\Delta d_{\parallel}\Delta \mathbf{D}_{\parallel} \quad (\text{S1.18})$$

$$\approx i\omega\varepsilon_0(\varepsilon_d - \varepsilon_m)\Delta d_{\parallel}\mathbf{E}_{\parallel}. \quad (\text{S1.19})$$

211 If we insert d_{\parallel} component perturbation Δd_{\parallel} from the main text, we obtain

$$\Delta \mathbf{K} \approx i\varepsilon_0 \frac{\omega_p^2}{\omega + i\gamma} \frac{\Delta \eta_0}{n_0} \mathbf{E}_{\parallel} \quad (\text{S1.20})$$

$$= \Delta \sigma_s \mathbf{E}_{\parallel} \quad (\text{S1.21})$$

212 This result is equivalent to one obtained from the classical surface model introduced by Bohren and Hunt (see
213 Eq. (S1.7)).

214 1.8 Effect of the d -parameters on the properties of plasmonic resonance

215 A small surface averaged perturbation in one of the d -parameters $\langle \Delta d_i \rangle$, where $i = \{\perp, \parallel\}$, will induce a change
216 in the scattering cross-section $\Delta_i \sigma_{\text{sca}}$. If we assume that each of the induced changes is smaller than the
217 unperturbed scattering cross-section $\Delta_i \sigma_{\text{sca}} \ll \sigma_{\text{sca}}$, we can treat them independently. Therefore, the total
218 change of scattering is given as the sum of the independent contributions

$$\Delta \sigma_{\text{sca}} = \sum_i \Delta_i \sigma_{\text{sca}}, \quad (\text{S1.22})$$

219 where the individual contributions are

$$\Delta_i \sigma_{\text{sca}} = \frac{\partial \sigma_{\text{sca}}}{\partial d_i} \langle \Delta d_i \rangle. \quad (\text{S1.23})$$

220 Additionally, we can express this change in terms of the influence on the eigenfrequency of the system as stated
221 with Eq. (2) in the main text. Assuming a lossy harmonic oscillator as a model for a plasmonic nanoresonator
222 relative change of the scattering cross-section near the resonance frequency can be modeled using the relative
223 change of the Lorentzian

$$\frac{\Delta \sigma_{\text{sca}}}{\sigma_{\text{sca}0}} \approx \frac{\Delta L}{L_0}. \quad (\text{S1.24})$$

224 We can express this change analytically and use it as a fitting curve as analyzed in SI section 1.1 as follows:

$$\frac{\Delta L}{L_0} = \frac{\Delta L_{\omega_r}}{L_0} + \frac{\Delta L_{\gamma_r}}{L_0} = L_0 \left[2(\omega - \omega_r)\Delta\omega_r - \frac{\gamma_r}{2}\Delta\gamma_r \right]. \quad (\text{S1.25})$$

225 Therefore, for each of the d -parameters we can obtain its impact on the resonance frequency $\Delta\omega_r$ and resonance
226 width $\Delta\gamma_r$ and retrieve the perturbation strengths $a_i = \Delta\omega_r / \langle \Delta d_i \rangle$.

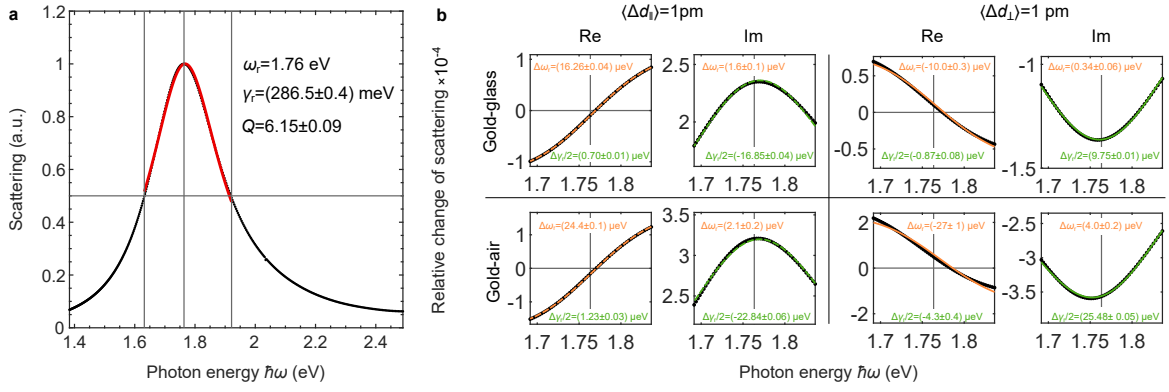


FIG. S3: **Influence of the d -parameter perturbations on the plasmonic resonance.** **a**, Scattering resonance (black) fitted with Lorentzian (red). **b**, Relative change of scattering fitted with relative change of Lorentzian for real and imaginary surface-averaged perturbations: left $\langle \Delta d_{\parallel} \rangle = 1$ pm, right $\langle \Delta d_{\perp} \rangle = 1$ pm, top gold-glass interface, bottom gold-air interface.

2 Experiment

2.1 Electro-optical setup

To measure the relative change of the scattering cross-section, we utilize an electro-optical setup, as depicted in Fig. S4. The setup is divided into two paths using a 50:50 beam splitter: the excitation path and the detection path. In the excitation path, we employ a tunable laser as the excitation source operating at the optical frequency ω . The laser light passes through a 300 μm pinhole which is imaged onto the back focal plane of the objective using a Fourier lens positioned before the beam splitter. A collimated beam is used to excite the structure, causing it to scatter light. The light reflected from the sample and scattered by the nanoresonator is guided through the detection beam path. Here, the reflected light is filtered out using a beam block. Additional filtering of the scattered signal is done by refocusing the scattered light to an intermediate image plane and using an iris to remove the stray light. The scattered light is then split using a 90:10 beam splitter, dividing the scattered light between the photodetector and the powermeter. The powermeter provides a direct readout, allowing us to obtain the unperturbed part of the scattered power P_0 . The signal from the photodetector is sent to a lock-in amplifier, enabling us to accurately measure the change in scattered power ΔP .

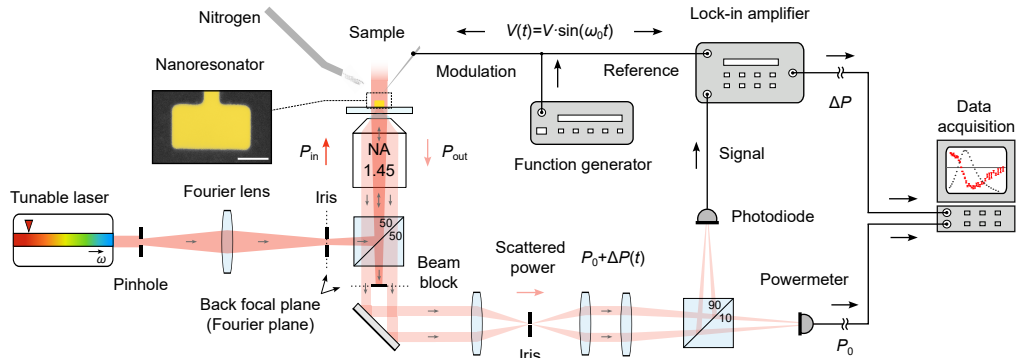


FIG. S4: **Experimental setup.** Schematics of electro-optical setup.

2.2 Scattering measurements

To determine the scattering cross-section, it is necessary to measure both the power scattered by the structure, P_s , and the excitation intensity, $I \approx P_{\text{in}}/r^2\pi$, where P_{in} represents the incoming power and r is the radius of the excitation spot. The typical beam size is approximately 1.5 μm , while the length of the longest nanoresonator is 180 nm. Therefore, it is assumed that the intensity is constant across the nanoresonator which justifies the use of a plane wave as an excitation source in simulations.

The nanoresonator is illuminated with light from the glass side, at angles below the critical angle. The power scattered by the nanoresonator P_s is measured by collecting the scattered light using the same objective that was used for excitation. The collection of light occurs at angles above the critical angle but below the maximum collection angle, which is determined by the numerical aperture (NA) of the objective.

To separate the light reflected from the sample from the scattered light, a circular patch is introduced in the back focal plane of the objective in the detection beam path. This circular patch effectively removes the reflected light. However, it is important to note that a small background signal persists due to the presence of stray light and scattering of light on imperfections present on the substrate. Consequently, the total scattered power, denoted as P , can be expressed as the sum of the power originating from the nanoresonator structure P_s , and the background scattered power P_b (see Fig. S5). Background signal is filtered out by focusing the light onto an intermediate plane and implementing an iris to eliminate scattering sources that are not in the proximity of the nanoresonator. To evaluate the impact of the residual background resulting from other scattering sources, we conduct measurements on a flat glass substrate while keeping the beam block in position. By measuring the signal under these conditions, we observe that the background power is negligible compared to the power

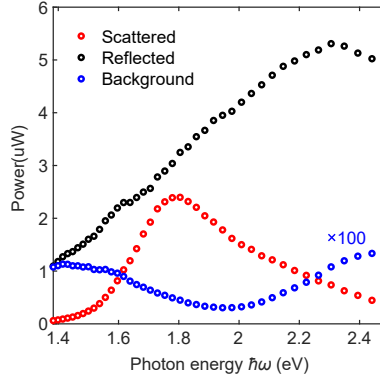


FIG. S5: **Measured scattered power.** Power of scattered signal (red), reflected signal (black) and background signal (blue).

261 scattered by the nanoresonator structure - it accounts only for a few percent of the total scattered power as
 262 shown in Fig. S5, indicating that $P_s \approx P$.

263 In order to determine the incoming intensity I , we begin by measuring the power of light that is reflected
 264 from a flat glass substrate, denoted as P_r , in the absence of the beam block. Assuming that the reflectance R
 265 remains constant across the spectral range, the incoming power can be determined up to a constant factor R as
 266 $P_r = RP_{in}$.

267 2.3 Characteristics of the excitation source

268 Spatial shape

269 To characterize the excitation source both spectrally and spatially, we direct the beam reflected from the sample
 270 directly to the spectrometer. Initially, we measure the shape of the beam, as depicted in Fig. S6a. By fitting a
 271 Gaussian function to the beam profiles in both the x and y directions, which are passing through the intensity
 272 maximum, we extract the corresponding beam widths, r_x and r_y . These beam widths are expressed in pixels,
 273 as illustrated in Fig. S6b. To obtain the frequency dependent beam size, denoted as \bar{r} , we calculate the average
 274 of these two beam widths. Subsequently, we calculate the spectral shape of the average intensity, denoted
 275 as I , which is inversely proportional to the square of the beam size. It can be mathematically expressed as
 276 $I \approx CP_r/\bar{r}^2$. Therefore, the intensity and scattering cross-section are determined up to a constant factor C

$$S = C \cdot \sigma_{sca} \approx \bar{r}^2 \frac{P}{P_r}. \quad (S2.1)$$

277 We refer to S as scattering signal. As a result, the relative change in the scattering cross-section i.e. scattering
 278 signal is equal to the relative change of the scattered power, that is

$$\frac{\Delta\sigma_{sca}}{\sigma_{sca0}} = \frac{\Delta S}{S_0} \approx \frac{\Delta P}{P_0}, \quad (S2.2)$$

279 where P_0 unperturbed scattered power. This provides us with the possibility to relate experimental data directly
 280 to the model.

281 It is important to note that each of the measured quantities is influenced by the setup transfer function T_s .
 282 However, when we take a quotient of these quantities, the effects of the transfer function cancel out.

283 Spectral shape

284 In an ideal scenario, it would be preferable to employ an excitation source, centered at frequency ω , with a zero
 285 spectral line width to precisely investigate the response of the nanoresonator at this optical frequency. However,
 286 in our setup, the excitation laser exhibits a non-zero spectral line width, as depicted in Fig. S6c. This introduces
 287 spectral distortion in the measurements due to the convolution of the true scattering cross-section and the

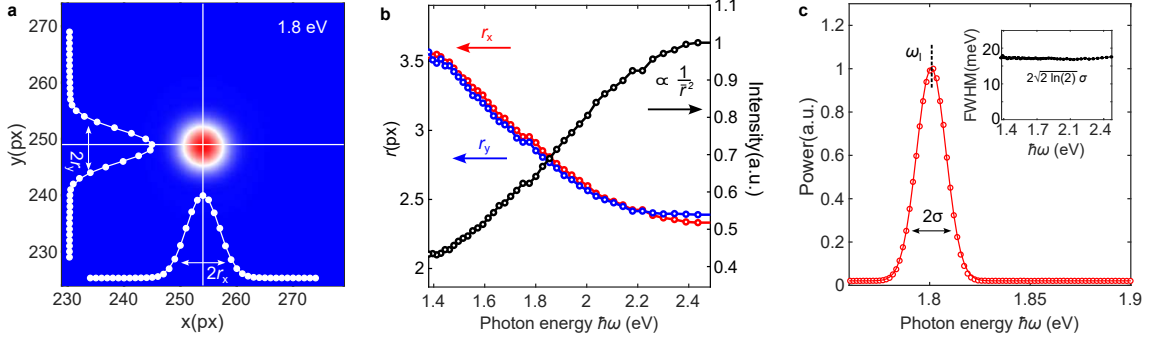


FIG. S6: **Characteristics of the excitation source.** **a** An image of the excitation beam is captured at 1.8 eV, after it reflects from a glass substrate. The image shows the beam profiles in the x and y directions. Gaussian curves are fitted to these profiles to determine the beam shape. **b** The beam sizes in the x and y directions are measured for different excitation frequencies. The average of the two beam sizes is used to calculate the intensity of the excitation source. **c** The source spectrum is obtained for a frequency of 1.8 eV. A Gaussian curve is fitted to the spectrum to determine the spectral line width. The spectral line width, is plotted as a function of the excitation frequency in the inset of the figure.

288 intensity given by a Gaussian function $I_G(\omega; \omega_1, \sigma) = I(\omega) \cdot G(\omega; \omega_1, \sigma)$, where ω_1 represents the peak position
 289 and σ represents the width of the Gaussian function. Consequently, the measured power will be affected by this
 290 spectral distortion

$$\begin{aligned}
 P'(\omega) &= (\sigma_{\text{sca}} * I_G)(\omega) = \int_{-\infty}^{\infty} \sigma_{\text{sca}}(\omega') \cdot I(\omega') \cdot G(\omega'; \omega, \sigma) d\omega' \\
 &= \int_{-\infty}^{\infty} P(\omega') \cdot G(\omega'; \omega, \sigma) d\omega' = (P * G)(\omega),
 \end{aligned}
 \tag{S2.3}$$

291 and to retrieve true scattered power $P(\omega)$ we need to deconvolute the measured signal. Figure S7 illustrates the
 292 scattering signal taking into account the excitation source characteristics. The plot presents two scenarios: one
 293 considering only the beam size (black circles) and another (blue line) considering both the beam size and the
 294 spectral line width. The results show that the beam size influences the shape of the calculated spectrum, while
 295 the spectral line width of the excitation source has minimal impact.

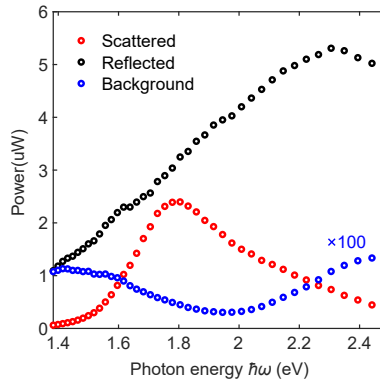


FIG. S7: **Measured scattering spectrum.** The scattering spectrum is plotted with and without considering the influence of the source characteristics. The red circles correspond to the measured spectrum without taking into account the source characteristics. The black circles represent the corrected spectrum, considering the non-constant intensity spectrum due to dispersive beam size. Additionally, the blue curve represents the spectral distortion caused by the non-zero linewidth of the excitation source.

2.4 Exemplary lock-in measurements

It is expected that the charge effect observed in lock-in measurements will only manifest at the fundamental frequency ν_0 i.e. frequency of the driving signal. Additionally, the signal should remain constant across the entire spectrum up to a frequency determined by the RC time of the system. At sufficiently low frequencies, only the in-phase component should be present, exhibiting a linear relationship with the applied voltage. These expectations have been experimentally validated, as depicted in Fig. S8. In panel a), the relative change in the scattering spectrum, measured at a driving frequency of $\nu_0 = 24$ kHz with an applied voltage of 10 V, clearly exhibits a purely in-phase component. Furthermore, panel b) demonstrates the absence of a lock-in signal at the second harmonic frequency $2\nu_0$. Panel c illustrates the linear scaling of the lock-in signal with applied voltage for three different optical frequencies, indicated by black arrows in panel a). Finally, panel d) exhibits the spectral dependence of the observed signal at ν_0 for the same three spectral points as in panel c). It can be observed that the signal remains constant above across the spectrum.

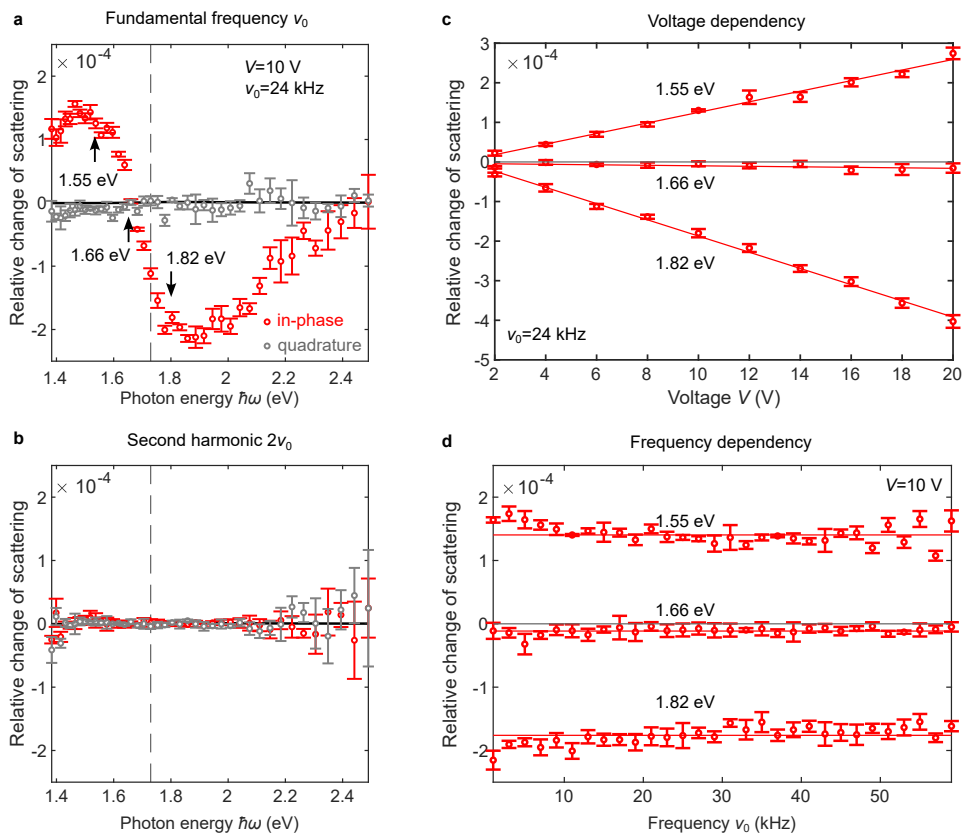


FIG. S8: **Exemplary lock-in measurements.** Spectral dependency of relative change of scattering for in-phase (red) and quadrature (gray) component for applied voltage of $V = 10$ V at **a**, driving(fundamental) frequency $\nu_0 = 24$ kHz and **b**, second harmonic frequency $\nu_0 = 2 \times 24$ kHz. **c**, Voltage dependency for three spectral points denoted with arrows in **a** at $\nu_0 = 24$ kHz. **d**, ν_0 frequency dependency for $V = 10$ V.

2.5 Changing the length of the nanoresonator

To investigate spectral dependency of perturbation we fabricate resonators with fixed width of 80 nm and vary length in steps of 20 nm between 180 nm and 100 nm, with resonances covering spectral range from 1.5 eV to 2 eV as shown in the Fig. S9a. We simulate equivalent systems and observe the similar trend for both peak position and resonance width, where longer structures show wider resonances (see Fig. S9b), attributed to the increase in radiation loss. Furthermore, the relative change of scattering exhibits a similar shape for all of the resonators Fig. S9c, with smaller structures showing increase in magnitude of maximum relative change. This can be assigned to both: spectral dependency of d -parameters, as well as increase in the relative change of

316 number of added electrons for the smaller systems. As already demonstrated with the exemplary measurement,
 317 the retrieved change of the resonance position, implying redshift for all of the structures, is in good agreement
 318 across the spectrum with classical expectations, where we consider only perturbation of parallel component.
 319 The addition of the perpendicular component obtained from DFT calculations, decreases the amplitude of the
 320 shift in resonance position but preserves the sign of change. However, significant difference between predictions
 321 based on both classical and DFT model and experiment is evident in the change of the width of the resonance.
 322 For positive bias, experimental results show a widening of the resonances for all of the structures, with a linearly
 323 increasing trend across the spectrum. One thing to note is that the classical model does predict minor increase
 324 of width past 2 eV. On the other hand including perturbations due to perpendicular component show significant
 325 decrease in loss when applying positive bias, which is in stark contrast compared to the experimental findings.

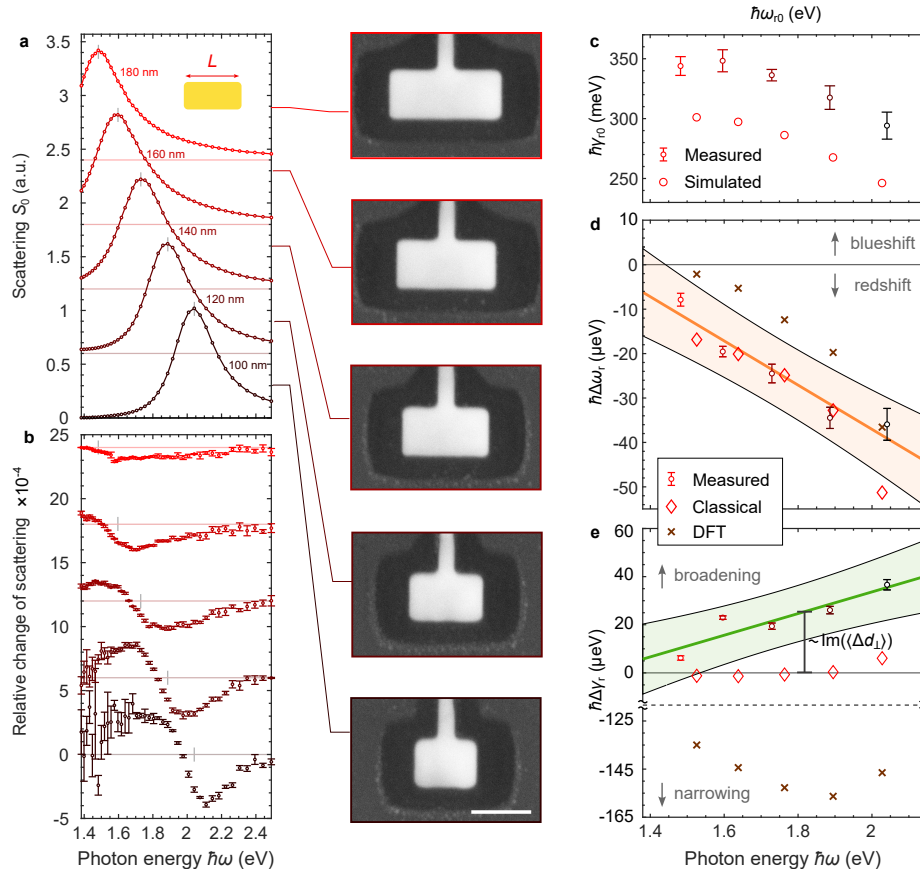


FIG. S9: **Tuning the nanoresonator.** **a**, Scattering spectrum for resonators with lengths ranging from 100 nm to 180 nm and corresponding SEM images. **b**, Relative change of scattering for resonators in **a**. **c**, Unperturbed resonance position and line width for resonators in **a** and corresponding simulated systems. **d**, Measured and simulated change of resonance frequency. **e**, Measured and simulated change of line width.

326 References

- 327 [1] Neil W Ashcroft and N David Mermin. *Solid state physics*. Cengage Learning, 2022.
- 328 [2] C. F. Bohren and A. J. Hunt. Scattering of electromagnetic waves by a charged sphere. *Canadian Journal*
329 *of Physics*, 55(21):1930–1935, 1977.
- 330 [3] J. Meier, L. Zurak, A. Locatelli, T. Feichtner, R. Kullock, and B. Hecht. Controlling field asymmetry in
331 nanoscale gaps for second harmonic generation. *arXiv:2210.14105*.
- 332 [4] T. Christensen, W. Yan, A.-P. Jauho, M. Soljačić, and N. A. Mortensen. Quantum corrections in nanoplas-
333 monics: shape, scale, and material. *Physical Review Letters*, 118(15):157402, 2017.
- 334 [5] P. J. Feibelman. Surface electromagnetic fields. *Progress in Surface Science*, 12(4):287–407, 1982.
- 335 [6] E. Hood and H. Metiu. Many-body phenomena at surfaces, edited by D. Langreth and H. Suhl, 1984.
- 336 [7] A. Varas, P. García-González, J. Feist, F. J. García-Vidal, and A. Rubio. Quantum plasmonics: from
337 jellium models to ab initio calculations. *Nanophotonics*, 5(3):409–426, 2016.
- 338 [8] P. J. Feibelman. Microscopic calculation of electromagnetic fields in refraction at a jellium-vacuum inter-
339 face. *Physical Review B*, 12(4):1319, 1975.
- 340 [9] R. C. Monreal, T. J. Antosiewicz, and S. P. Apell. Diffuse surface scattering and quantum size effects in
341 the surface plasmon resonances of low-carrier-density nanocrystals. *The Journal of Physical Chemistry*
342 *C*, 120(9):5074–5082, 2016.
- 343 [10] M. K. Svendsen, C. Wolff, A.-P. Jauho, N. A. Mortensen, and C. Tserkezis. Role of diffusive surface
344 scattering in nonlocal plasmonics. *Journal of Physics: Condensed Matter*, 32(39):395702, 2020.
- 345 [11] N. A. Mortensen, P. A. D. Gonçalves, F. A. Shuklin, J. D. Cox, C. Tserkezis, M. Ichikawa, and
346 C. Wolff. Surface-response functions obtained from equilibrium electron-density profiles. *Nanophotonics*,
347 10(14):3647–3657, 2021.
- 348 [12] Y. Yang, D. Zhu, W. Yan, A. Agarwal, M. Zheng, J. D. Joannopoulos, P. Lalanne, T. Christensen, K. K.
349 Berggren, and M. Soljačić. A general theoretical and experimental framework for nanoscale electromag-
350 netism. *Nature*, 576(7786):248–252, 2019.